Elsevier Editorial System(tm) for Journal of Sound and Vibration

Manuscript Draft

Manuscript Number: JSV-D-19-01748R1

Title: Physical mechanisms and performance of slitted leading-edge profiles for the reduction of broadband aerofoil interaction noise

Article Type: Full Length Article

Section/Category: G Acoustics/vibroacoustics

Keywords: aeroacoustics, aerofoil noise, serrations

Corresponding Author: Miss Marine Cannard,

Corresponding Author's Institution: ISVR

First Author: Marine Cannard

Order of Authors: Marine Cannard; Phillip Joseph; Jacob Turner; Jae Wook Kim; Paruchuri Chaitanya

Abstract: Aerofoil Turbulence Interaction (ATI) noise is an inviscid phenomenon generated by the impingement of turbulent flows onto the leading-edge of an aerofoil. This paper deals with a novel leading-edge serration geometry, composed of narrow slits, to reduce ATI noise. These profiles have been recently found to provide significantly better noise reductions than conventional leading edge geometries. A numerical and analytic investigation is performed into the mechanism and performance of its noise reduction. The far-field radiation is shown to be influenced by a system of induced vortices affecting the distribution of sources on the flat-plate and by destructive interference between the two sources generated at both ends of the slit. A simple two-source model is developed to predict the far-field noise reduction obtained and compared to straight leading-edge aerofoils.

Physical mechanisms and performance of slitted leading-edge profiles for the reduction of broadband aerofoil interaction noise

Marine Cannard[a,*], Phillip Joseph[a], Jacob Turner[b], Jae Wook Kim[b], Paruchuri Chaitanya[a]

[a] *Institute of Sound and Vibration Research, University of Southampton, Southampton, SO17 1BJ, UK*
[b] *Aerodynamics and Flight Mechanics Research Group, University of Southampton, Southampton, SO17 1BJ, UK*

Abstract

Aerofoil Turbulence Interaction (ATI) noise is an inviscid phenomenon generated by the impingement of turbulent flows onto the leading-edge of an aerofoil. This paper deals with a novel leading-edge serration geometry, composed of narrow slits, to reduce ATI noise. These profiles have been recently found to provide significantly better noise reductions than conventional leading edge geometries. A numerical and analytic investigation is performed into the mechanism and performance of its noise reduction. The far-field radiation is shown to be influenced by a system of induced vortices affecting the distribution of sources on the flat-plate and by destructive interference between the two sources generated at both ends of the slit. A simple two-source model is developed to predict the far-field noise reduction obtained and compared to straight leading-edge aerofoils.

Keywords: Aeroacoustics, aerofoil noise, serrations

1. Introduction

Aerofoils have a wide range of applications, from aircraft engines to wind turbines and industrial fans. A dominant noise generation mechanism on

*m.cannard@soton.ac.uk

aerofoils occurs through the interaction between turbulent flow and the aerofoil leading-edge. ATI is an inviscid phenomenon in which vorticity is scattered at the leading edge into sound. On a modern turbofan engine, ATI noise is believed to be the dominant broadband noise source and is generated through the impingement of turbulent wakes from the rotor interacting with the outlet guide vanes. Over the last decade, modifications to the OGV aerofoil geometry have been tested and developed as a passive treatment to reduce ATI noise. Experimental and numerical studies have shown that modifications to leading-edge geometries, such as thickness, camber or nose radius are not effective in reducing ATI noise [1]. One of the most promising methods of reducing ATI noise is by the introduction of serrations, or undulations, onto the aerofoil leading-edge. However, nearly all of these previous studies on leading-edge serrations have been restricted to sinusoidal or sawtooth profiles. This problem has been investigated analytically ([2–4]), using Computer Fluid Dynamic computations ([5–9]) and experimentally ([10–13]). The upper bound limit on the performance of these simple profiles was identified by Chaitanya [1]. They showed that, for best performance, the serration wavelength must be four times the turbulence integral length-scale. Under this condition, Chaitanya has shown that the sound power reduction ΔPWL closely follows $\Delta\text{PWL} = 10\log_{10}(fh/U) + 10$, where h is the serration peak-to-peak amplitude and U the mean flow speed.

A recent experimental study has demonstrated the increased effectiveness of a new family of leading edge profiles for reducing ATI noise [14] compared to these sinusoidal profiles. One of the most promising of these new profiles simply comprises the introduction of narrow rectangular slits onto the leading-edge. Typical sound power level reductions versus non-dimensional frequency fh/U, where h is the slit length, obtained by placing the aerofoils in the open jet wind tunnel facility at the ISVR, in an isotropic turbulent flow, is shown in Fig. 1. The solid blue and red curves in this figure represent the noise reductions due to the slits on a flat plate and a NACA65 aerofoil respectively. Also shown in the figure as a dashed line is the function $10\log_{10}(fh/U) + 10$ representing the noise reduction due to a sinusoidal serration of amplitude h. Clearly, the slitted profile can be seen to provide significantly better noise reductions than the conventional profile at low frequencies while generally providing smaller noise reductions at high frequencies due to trailing edge interaction [15]. A characteristic feature of the noise reduction spectra plotted in Fig. 1 is the appearance of three peaks very close to the Strouhal frequencies of $fh/U = 0.5$, 1.5 and 2.5. This con-

dition implies a phase difference of π, $3\pi/2$ and $5\pi/2$ respectively between two compact sources at either end of the slit of approximately equal source strength. The most likely interpretation of this finding therefore is that the peaks are the result of destructive interference between these two sources. This hypothesis will be confirmed in the numerical surface pressure predictions presented below However, the detailed mechanism by which these very narrow slits can produce source strengths at the end of the slit that are comparable to the leading edge is not known and is one of the subjects of this paper.

This paper focuses on a numerical study into the characteristics and mechanism of the noise reduction due to slitted leading edges interacting with turbulent flow. In this study, the aerofoil is modelled as a flat-plate located in a uniform mean flow at zero angle of attack. We consider the interaction of the flat plate with a single spanwise vortex injected upstream. Simulations are performed using an optimized high-order finite-difference solver, which solves the full 3D compressible Euler equations in the time-domain. The surface pressure fluctuations generated on the slitted flat-plate and the far-field radiated noise are analysed in detail and compared to results obtained with a straight leading-edge. Preliminary simulation results of the secondary vorticity generated by the slitted flat plate was presented by [16] for a comparatively short slitted flat plate at an initial attempt at explaining the noise reduction mechanism. In the present paper, the vortex dynamics is explored in greater detail as well as a detailed investigation into the resulting unsteady surface pressure distribution. Special attention is paid to the identification of the noise reduction mechanism. A simple two-source model is developed to predict the far field radiation from the slitted aerofoil and shown to provide very close agreement with the noise reduction obtained by the exact calculation. The model is analysed to determine observer angles of maximum noise reduction.

We first provide a description of the serration geometry, followed by the details on the computational procedure used in the investigation. The source distribution in the vicinity of the slit and its generation mechanism will be analysed. Finally, the far field radiation is investigated based on an exact integration of the surface pressure and an approximation in terms of two interfering compact sources at either end of the slit.

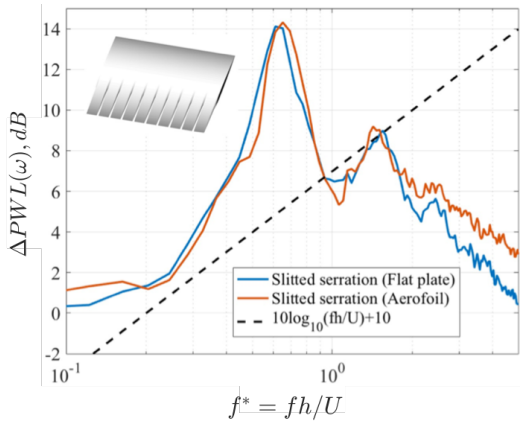

Figure 1: Sound power reduction comparisons for a slitted serration on flat plate and aerofoil of amplitude-chord ratio ($h/c_0 = 0.167$), width-wavelength ratio $w/\lambda = 0.133$ at jet velocity of 60 m/s [14]

2. Serration geometry and computational setup

2.1. Definition of the problem

The numerical study is performed on a semi-infinite flat plate with zero thickness being impacted by a vortical disturbance injected upstream of the aerofoil. A uniform mean flow velocity is assumed with free stream Mach number set to $M = 0.3$, oriented in the chordwise x-direction. The aerofoil chord is effectively semi-infinite by extending further downstream the no-slip (no-penetration) boundary conditions implemented on the flat-plate. This condition allows the removal of trailing edge interaction noise. A rectangular slit has been introduced onto the flat-plate leading-edge by applying the no-slip boundary condition to the grid points located on the edges of the slit where all velocity components vanish. The situation is depicted in Fig. 2 indicating a rectangular slit of width w along the x_3-direction and length h along the x_1-direction, with x_2 the direction normal to the plate. Periodic boundary conditions are applied across the spanwise boundary planes of the flat plate separated by λ. The total plate span is therefore effectively infinite so that the slit is repeated every wavelength λ. Note that all positions and lengths are normalised by unit length and all velocities are normalised by the speed of sound.

The vortical disturbance impinging on the flat plate is modelled as a single spanwise vortex injected upstream of the plate through the use of a

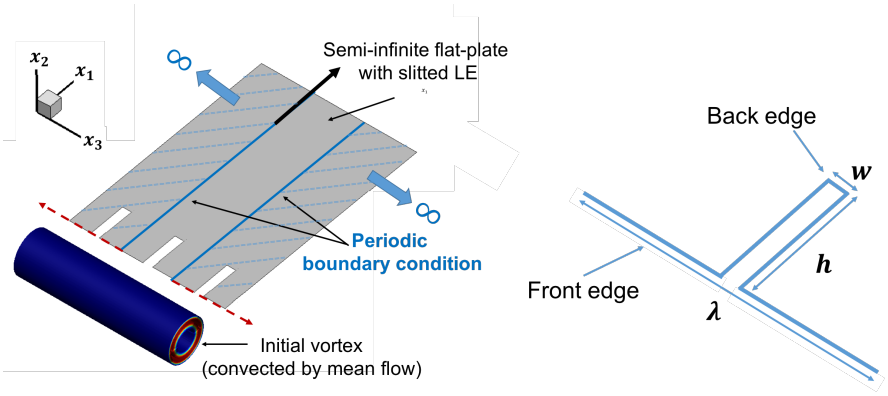

Figure 2: Sketch of the current problem (the red dotted arrow indicates periodic boundary conditions in the spanwise direction)

sponge zone. The vortex model is based on the Gaussian eddy profile used in the synthetic turbulence model proposed by [17] and [7]. The vortex-induced velocity field at point in the field $\mathbf{x} = (x_1, x_2, x_3)$ is determined by taking the curl of a vector potential shape function $\psi(\mathbf{x})$ ($\mathbf{u}'(\mathbf{x}, t = 0) = \nabla \times [\psi(\mathbf{x})\mathbf{e}_z]$), where $\mathbf{e}_z$ is a unit vector in the spanwise direction. This ensures that the vortex is divergence-free, which is essential to avoid the production of spurious noise. The Gaussian shape function ψ is described in Eq. (1), where c is the speed of sound, and is completely defined by the two parameters $\sigma_{vortex} = 0.001$ and $\epsilon_{vortex} = 0.24$, which control the vortex size and strength respectively. These parameters give a vortex velocity amplitude close to 2% of the mean flow to minimise non-linear propagation effects.

$$\psi(\mathbf{x}) = c\frac{\epsilon_{vortex}}{\sqrt{\sigma_{vortex}}} \exp\left(-\left[3\sigma_{vortex} r^2(\mathbf{x})\right]^2\right), \qquad r^2(\mathbf{x}) = (x_1 - x_0)^2 + x_2^2 \quad (1)$$

Taking the curl of the shape function defined in Eq. (1) gives the following expressions for the streamwise and transverse components, $\mathbf{u}$ and $\mathbf{v}$ of the initial velocity field, given in Eq. (2), where $x_0 = -1.355$ is the prescribed initial position of the vortex core and $x_{\mathrm{LE}} = -0.5$ the location of the plate leading-edge.

$$\left.\begin{aligned} \mathbf{u}(\mathbf{x}, t = 0) &= U - 36\sigma^2 x_2 r(\mathbf{x})\psi(\mathbf{x}) \\ \mathbf{v}(\mathbf{x}, t = 0) &= 36\sigma^2 (x_1 - x_0) r(\mathbf{x})\psi(\mathbf{x}) \end{aligned}\right\} \quad (2)$$

In this study we assume that the incoming disturbance is a single 2D spanwise vortex whose velocity components are therefore identical along the span. The limitation with this 2D approach is that the effects of spanwise correlation and the stochastic features of the incoming turbulence are not included. However, the 2D vortex has the significant advantage that it allows secondary vortices to be easily identified, its frequency spectrum is smoothly varying, and does not require time averaging. The use of a single vortex therefore allows one to focus on the fundamental slit response. The essential difference between incoming turbulent flow and the single vortex assumed in this paper is that in the case of turbulence the surface pressure response between adjacent slits is likely to be partially coherent while it is perfectly coherent for a single 2D incoming vortex. Furthermore, we anticipate that the effect of turbulence length scale on the noise reductions will be small when the slit width is smaller than the turbulence length scale. The essential noise reduction mechanism for each slit is therefore identical in both cases. The transverse velocity profile (normal to the plate) of the initial vortex, along the centre-line is plotted in Fig. 3 versus non-dimensional streamwise position x_1. The vortex is assumed to rotate in the clockwise direction as it convects downstream. The vortex can be seen to first generate a downward stroke as it encounters the flat plate, followed by an upward stroke with identical velocity. As the vortex convects over the flat plate, positive pressure is generated during the downward stroke on the upper side of the plate followed by negative pressure during the upwards stroke, with the opposite behaviour occurring on the lower side.

The Power Spectral Density $\Phi_{vv}(\omega)$ of the transverse velocity fluctuation v defined in Eq. (2) is plotted in Fig. 3 versus non-dimensional frequency $f\Lambda/U$ based on the assumption that the eddy convects as a frozen pattern with mean flow speed U. We note that even though the vortex shape is unbounded and decays exponentially from its centre, it will be shown to be useful to define the effective radius of the vortex Λ in a manner consistent with the integral length scale for turbulence, given by Eq. (3). The leading edge of the vortex is therefore assumed to be located at Λ from the vortex centre, which is the initial position of the vortex, referred to as x_0 in 3.

$$\Lambda = \frac{1}{\max|v(x_1)|}\int_{x_0}^{x_0+\infty}|v(x_1)|\mathrm{d}x_1 \quad \text{at} \quad x_2 = x_3 = 0, t = 0 \tag{3}$$

This paper will focus on a representative slit configuration based on typ-

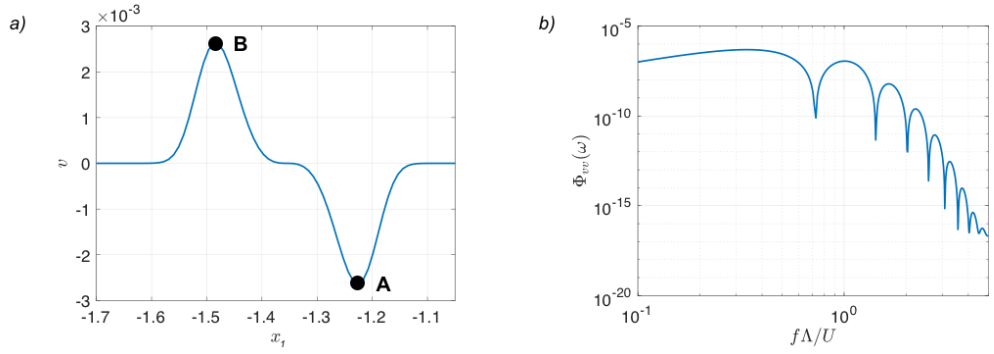

Figure 3: Prescribed vortex velocity at $t = 0$ (a) and power spectral density of the transverse velocity fluctuation versus non-dimensional frequency (b). Point A and point B indicate the location of maximum downwash and maximum upwash respectively

ical dimension ratios investigated experimentally by Chaitanya [14]. It has a slit aspect ratio of $h/w = 33$ with $\lambda/w = 10$, where λ is determined by the periodic boundary condition. These parameters capture the essential physics of the noise reduction mechanism. Before presenting the predictions of the noise reductions obtained by the slit we first provide an overview of the numerical procedure used to determine both the surface pressure fluctuations and its far field radiation.

2.2. Wall surface pressure

In order to determine the noise reduction mechanism it is first necessary to predict the variation of unsteady pressure over the surface of the flat plate. This information will also be used in this paper to predict the far field radiation. The wall pressure generated by the vortical disturbance on the flat-plate is determined by a 3D compressible Euler time-domain solver, using optimized high-order finite-difference compact schemes and filters ([18, 19]). Viscosity effects are therefore neglected in these simulations. This inviscid hypothesis has been assumed in all previous numerical investigations into the noise reductions due to serrated leading edge profiles, for example ([5–8]). For the particular case of the narrow slit, viscosity is likely to have some influence on the behaviour of the flow in the vicinity of the slit. However, we will demonstrate that this inviscid simulation provides good qualitative agreement with the noise reductions obtained experimentally in Fig. 1, thereby demonstrating that the simulation is capable of capturing the essential noise

reduction mechanisms.

The governing equations are solved in conservative form and expressed in a generalized coordinate system as given by Eq. (4):

$$\frac{\partial}{\partial t}\left(\frac{E}{J}\right)+\frac{\partial}{\partial \xi_i}\left(\frac{F_j}{J}\frac{\partial \xi_i}{\partial x_j}\right)=-c\frac{S}{J} \tag{4}$$

where E and F respectively represent the conservative variable and flux vectors and are defined by

$$E=\begin{bmatrix}\rho\\ \rho u\\ \rho v\\ \rho w\\ \rho e_t\end{bmatrix};\quad F_j=\begin{bmatrix}\rho u_j\\ \rho u u_j+\delta_{1j}p\\ \rho v u_j+\delta_{2j}p\\ \rho w u_j+\delta_{3j}p\\ (\rho e_t+p)u_j\end{bmatrix}. \tag{5}$$

with $e_t = p/\left[(\gamma-1)\rho\right] + u_j u_j/2$ the internal energy per unit mass and $u_j = \{u, v, w\}$ the fluctuating velocity field. The generalized coordinates are given by $\xi_i = \{\xi, \eta, \zeta\}$, while the Cartesian system is represented by $x_j = \{x_1, x_2, x_3\}$ with $i = 1, 2, 3$ and $j = 1, 2, 3$. The Jacobian determinant of the coordinate transformation from Cartesian to generalized coordinates is given by $J = |\partial(\xi, \eta, \zeta)/\partial(x, y, z)|$. An additional source term S is included on the RHS of the governing equations in Eq. 4 and represents the sponge zone surrounding the computational domain used to inject the initial vortex. The sponge zone is also used as an absorbing treatment to attenuate the acoustic waves towards the outer boundaries and prevent numerical reflections.

The simulation is realised on a total of $802 \times 602 \times 101$ grid cells in the x_1, x_2 and x_3 directions respectively, corresponding to a total of 48, 763, 204 grid cells in the domain, which are shared over 480 processor cores for parallelisation purposes.

The computational domain is decomposed into 6 blocks arranged in a H-topology. The use of a multi-block grid facilitates the meshing of complex regions and introduces greater efficiency in running the code in parallel. In the present analysis, the chosen grid is Cartesian, with a clustering of points at specific regions of the computational domain to capture the main important features of the flow. The grid spacing is reduced upstream of the aerofoil to resolve adequately the vortex with at least 25 points across the vortex radius, but stretched in regions where the flow is fully developed to balance

the use of computational resources. In order to capture the main characteristics of the physical mechanisms, the mesh has a greater refinement in all directions near the slit. In the spanwise x_3-direction, grid points are clustered around the slit corner with the smallest grid size $\Delta x_3^{min} = 0.001h$ and at least 30 points are used inside the slit. The grid is also refined in the streamwise (x_1) and transverse (x_2) directions, with the smallest cells located at the slit corners of size $\Delta x_1^{min} = \Delta x_2^{min} = 0.003h$. Finally, a total of 301 equidistant points are used along the slit streamwise edge to capture the development of secondary streamwise vortices. The grid parameters were chosen following a thorough grid convergence study on the number of points required inside the slit and around the slit corners to obtain a converged solution. The fine mesh used in this study is due to the need to resolve the detailed behavior of the secondary vortex system described in Section 3.

2.3. Validation with Amiet's flat plate model

By way of validation of the numerical procedure described above the pressure jump across the flat plate with Straight Leading Edge (SLE) was first computed. The predictions in time were Fourier Transformed to determine the magnitude and phase of the pressure jump at a single non-dimensional frequency $fL/c = 1.5$, where $L = 1$m, and the results plotted in Fig. 4 against non-dimensional distance x plotted on a logarithmic scale. Also shown in this figure is the predictions obtained from Amiet's model [20] of leading edge noise from a flat plate, by allowing the chord length to go to infinity. Note that since the aerofoil chord is essentially infinitely long, no trailing-edge correction was applied. Good overall agreement between the numerical and analytic predictions is observed.

The phase variation across the flat plate is consistent with a wave traveling downstream at a speed of $c+U$, indicating that the response of the flat plate is of the form of an acoustic wave superimposed on the mean flow.

2.4. Far-field radiation

The far-field radiation as a function of time $p(\mathbf{x}, t)$ at any observer $\mathbf{x}$ is determined directly by the integration of the fluctuations in pressure jump $\Delta p(\mathbf{y}, \tau)$ at all point $\mathbf{y}$ across the aerofoil surface, assuming dipole radiation into free space with uniform mean flow [21] and is therefore of the form,

$$p(\mathbf{x}, t) = -\frac{1}{2\pi} \iint_S \left[\Delta p(\mathbf{y}, \tau) \frac{\partial}{\partial y_2} G(\mathbf{x}, t|\mathbf{y}, \tau) \right] \mathrm{d}S(\mathbf{y}) \tag{6}$$

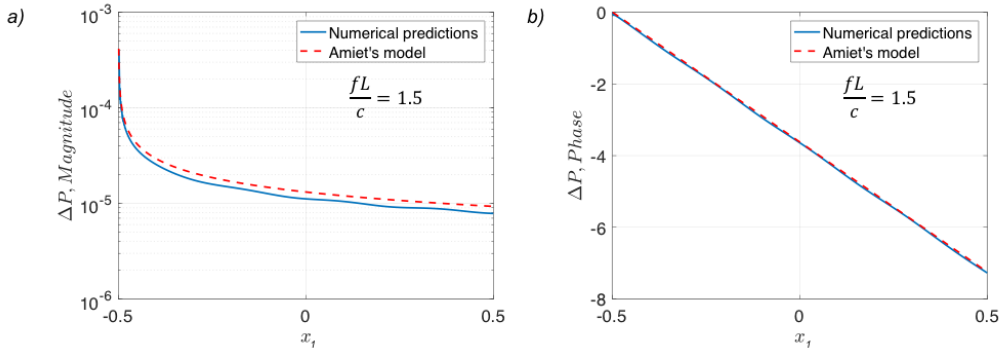

Figure 4: Magnitude (a) and phase (b) of the pressure jump along the chord for a straight leading-edge aerofoil - $fL/c = 1.5$

where $G(\mathbf{x}, t|\mathbf{y}, \tau)$ is the time-domain Green function between a source point $\mathbf{y}$ at source time τ and an observer at $\mathbf{x}$ at receiver time t given by,

$$G(\mathbf{x}, t|\mathbf{y}, \tau) = -\frac{\delta(\tau - t + \tau^*)}{4\pi r_\beta} \;\; ; \;\; \tau^* = \frac{r_\beta - M r_1}{c\beta^2} \tag{7}$$

in which $r_\beta = \sqrt{(x_1 - y_1)^2 + \beta^2(x_2 - y_2)^2 + \beta^2(x_3 - y_3)^2}$ represents the flow-corrected acoustic distance, $r_1 = |x_1 - y_1|$ and $\beta^2 = 1 - M^2$.

Finally, assuming far field observers the distance r_β is taken outside of the surface integral and replaced by $\sigma = \sqrt{x_1^2 + \beta^2(x_2^2 + x_3^2)}$. In the far field r_β can be approximated by $r_\beta \approx \sigma - \frac{x_1 y_1 + \beta^2 x_3 y_3}{\sigma}$ in the expression for the time delay τ^*, and near field terms of second order in r_β^2 can be neglected. The final expression for the acoustic pressure at an arbitrary far field observer can be expressed by Eq. (8).

$$p(\mathbf{x}, t) = -\frac{x_2}{4\pi c \sigma^2} \iint_S \left[\frac{\partial \Delta p(\mathbf{y}, \tau)}{\partial \tau}\right]_{\tau = t - \tau^*} \mathrm{d}S(\mathbf{y}) \tag{8}$$

where the pressure jump is evaluated at the retarded time $\tau = t - \tau^*$.

3. Source distribution on the flat-plate

3.1. Wall pressure fluctuations on the surface

For the purposes of understanding the noise reduction mechanism this section focuses on the time variation of pressure generated on the aerofoil

surface as the vortex convects across the plate. Contour plots of the pressure generated on the slitted and baseline aerofoil surfaces are shown in figures 5(a - f) corresponding to three instances in time during the passage of the vortex.

In this simulation the length of the slit was chosen so that $h/2\Lambda$=0.91. The first snapshot in time shown in Fig. 5(a) was chosen to correspond to when the maximum downwash velocity due to the vortex, identified as A in Fig. 3(a), reaches the front edge of the slitted flat plate. Also shown in Fig. 5(d) for comparison is the corresponding surface pressure distribution for the baseline aerofoil. The distribution of the surface pressure due to the slit can be clearly seen to more localised towards the leading edge than the baseline case. A strong span-wise pressure variation is now evident with the pressure dropping to very low values near the edges of the slit. The overall effect of the slit is therefore to provide a reduction in the integrated source strength, which will be considered in greater in detail below.

The second snapshot of time considered here corresponds to when the effective leading edge Λ of the vortex just arrives at the back edge of the slit so that the slit front edge simultaneously interacts with the vortex trailing edge. Highly localised, high intensity pressure fluctuations can be observed at the back edge of the slit. The level of pressure fluctuation in this region is significantly higher than the pressure fluctuation near the leading edge of the baseline aerofoil, which will be shown in Section 4 to contribute to the far field noise reduction. There therefore exists a range of angles for which the sound radiation from the front and back regions interfere destructively, leading to enhanced noise reductions. The conditions for destructive interference will be investigated in detail in Section 4. However, as confirmed at the end of Section ... the condition for destructive interference does not require the slit length to be shorter than the vortex size or length scale in the case of incoming turbulence.

Finally, the third snapshot in time considered here, plotted in Fig. 5(c), is when the effective trailing edge of the vortex just reaches the back edge of the slit. At this moment in time the distribution of pressure at the end of the slit closely matches that observed in Fig. 5(b) but with opposite sign since the velocity is now in the opposite direction.

Before investigating the relationship between the surface pressure fluctuations plotted in Fig. 5 and its far field radiation we first study the physical mechanisms responsible for these surface pressure distributions.

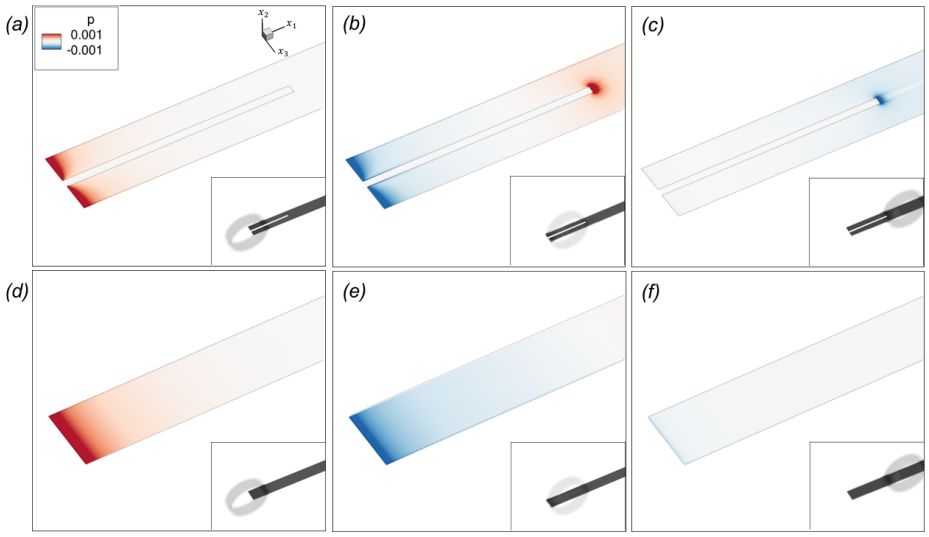

Figure 5: Contour plots of the generated acoustic pressure (p') on the aerofoil surface in temporal order: comparison slitted aerofoil ((a), (b), (c)) and baseline SLE ((d), (e), (f)). The iso-surfaces of the spanwise vorticity are represented with an additional scale on the right hand side corner to visualise the position of the main vortex

3.2. Influence of secondary vortices

As explained above, the generation of the two sources at the front and back-edge of the slit is due to the impingement of the main prescribed vortex on the plate. However, the respective level and shape of these acoustic regions can be linked to the influence of secondary vortices generated during the impingement of the main prescribed vortex onto the flat plate. Figures 6(a, b, c) show iso-surfaces of the induced spanwise and streamwise vortices created at the same three instants in time as Fig. 3. The no-slip boundary condition applied to the flat-plate leads to large velocity gradients in the vicinity of the slit. Strong secondary spanwise vorticity at the front and back edges can be observed, driven by the velocity gradient ($\partial v/\partial x_1 > 0$). Also present is strong secondary streamwise vorticity along the edges of the slit driven by the velocity gradient ($\partial v/\partial x_3 > 0$).

The generation of secondary vorticity was previously identified on wavy leading-edges by Turner [8] who attributed an increase in pressure at the root and a reduction in pressure at the peak to an additional downwash and counter-acting upwash respectively created by secondary vorticity. As pre-

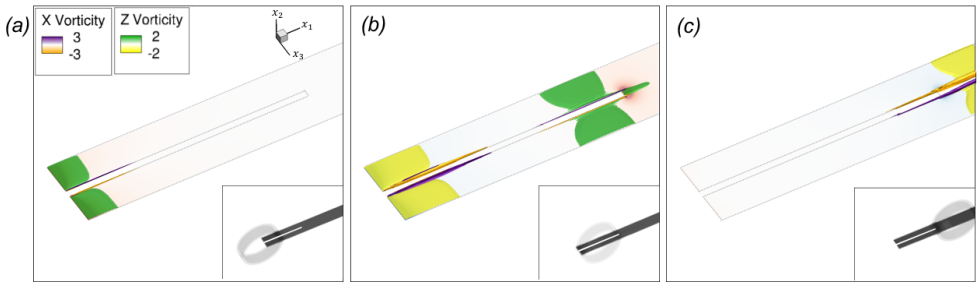

Figure 6: Contour plots for generated acoustic pressure (p') and iso-surfaces of induced vorticity generated along the leading-edge profile during the interaction, in temporal order. The iso-surfaces of the spanwise vorticity are represented with an additional scale on the right hand side corner to visualise the position of the main vortex

viously demonstrated by [8], the secondary spanwise vorticity on a serrated flat plate creates an additional downwash, contributing to higher pressure fluctuations, as it is also the case for a straight leading-edge aerofoil. An identical mechanism is encountered on slitted flat-plates, at both the front and the back-edge of the slit.

3.2.1. Influence of secondary streamwise vortices on the slit front-edge

For slitted aerofoils, in addition to the induced spanwise vortices, a streamwise vortex system can also be seen that originates at the slit corners and arises from the streamwise velocity discontinuity in the spanwise direction x_3 ($\partial v/\partial x_3 > 0$) across the longitudinal slit edge. Figures 6 (a, b) show the iso-surfaces of secondary streamwise vortices generated at the front and back edge of the slit when the main vortex impinges on the front and back edge respectively. A counter-rotating pair of streamwise vortices can be observed along the longitudinal edges of the slit which grows as the vortex is convected along the plate.

Figure 7(c) represents an illustration of the streamwise vortex system over a $x_2 - x_3$ plane at a specific streamwise location and shows their rotation direction. It indicates the generation of an upwash velocity that counteracts the downwash of the main vortex. As a result the pressure jump along the front-edge decreases as the slit corner is approached as indicated on Fig. 7(a). This is consistent with the spanwise decay of the pressure observed on Fig. 5 b).

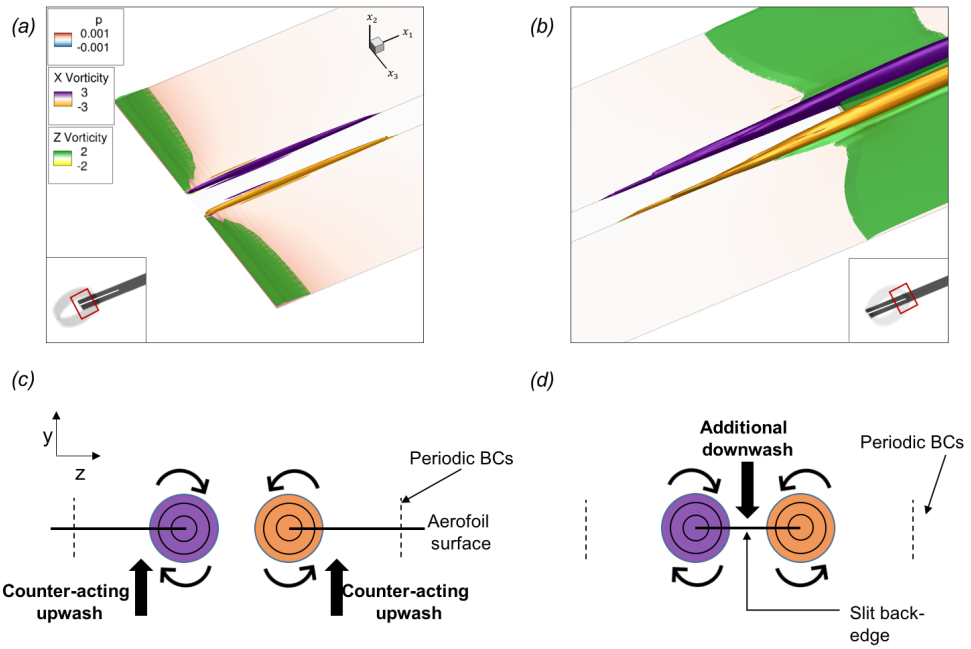

Figure 7: Influence of the counter-rotating pair of secondary streamwise vortices generated during the downwash of the main vortex: (a) zoom on the leading-edge as the main vortex impinges on the front-edge - (b) zoom on the back-edge as the main vortex impinges on the back-edge - (c) illustration of the streamwise vortices rotation at the front-edge - (d) illustration of the streamwise vortices rotation at the back-edge

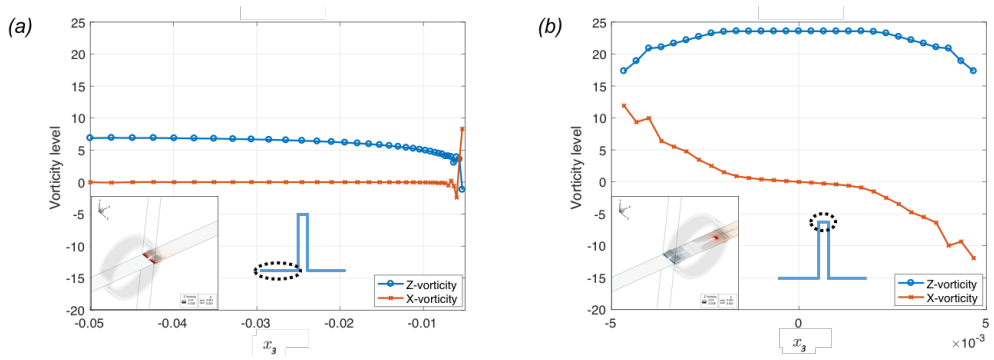

Figure 8: Spanwise and streamwise vorticity levels as the maximum downwash velocity (point A on Fig. 3 (a)) reaches the slit front edge (a) and the slit back-edge (b)

3.2.2. Influence of secondary streamwise vortices on the slit back-edge

We now consider the detailed variation in secondary vortex strength along the front and back edges. Fig. 8(a) shows the variation of spanwise and streamwise vorticity amplitudes along the span at the front-edge of the slit, as the location of maximum downwash (point A in Fig. 3(a)) just reaches the front edge. Similarly, Fig. 8(b) shows the variation in vorticity amplitudes along the back-edge of the slit as point A reaches the back edge. The comparison between Fig. 8(a) and Fig. 8(b) shows that both vorticity components are significantly larger at the back-edge than at the front for most of the span, except close to the front corner where the streamwise vorticity is generated and therefore reaches comparable levels to the levels at the back. Additionally, as indicated by Fig. 7(d), the downwash produced as the main vortex impinges on the back-edge of the slit is enhanced by the additional downwash created by the secondary streamwise vortices. This combined effect is responsible for the significantly higher pressure fluctuations observed at the back-edge of the slit.

It can be noted that the pressure fluctuations at the back-edge of the slit are likely to vary with the slit length, depending on the level of the streamwise vorticity reaching the back-edge. The source level at the back-edge will therefore vary with slit length, but the generation mechanism remains the same.

4. Two-source analytic model

Chaitanya [14] has proposed two noise reduction mechanisms to explain the enhanced noise reductions due to slitted aerofoils. One is related to a reduction in overall source strength, the other is related to interference between two highly coherent sources at either ends of the slit of roughly the same strength. Section 3 has confirmed the presence of two regions of very localised pressures at either ends of the slit.

Based on the hypothesis of two compact coherent sources Chaitanya has proposed a model for predicting sound power reductions at any arbitrary frequency. The model was aimed at explaining his experimental observations which showed that maximum sound power reductions were obtained at frequencies f_n for which $f_n h/U = (2n+1)/2$, where n is any integer $n = 0, 1, 2...$, as shown in Fig. 1. This observation provided evidence of strong interference between two compact source regions at either ends of the slit, which was used as the basis of the model. However, the model provides no insight into the effect of the slits on the detailed far field pressure directivity. Furthermore, in this frequency domain model, it was not possible to predict the condition for maximum overall noise reductions when integrated over all frequencies.

In this section we develop further the simple two-source model for predicting the noise reductions and also to assist in the understanding of the detailed noise reduction mechanism.

4.1. Derivation of the analytic model

The surface pressure distribution shown in Fig. 5 reveals the presence of two distinct source regions; one at the leading edge and another localised around the serration root. The integration of the surface pressures required to compute the far field radiation in Eq. (8) is therefore the sum of the surface integrations taken over their respective source areas S_F and S_B as illustrated in Fig. 9,

$$p(\mathbf{x},t) = -\frac{x_2}{4\pi c\sigma^2}\left[\iint_{S_\mathrm{F}} \frac{\partial \Delta p(\mathbf{y},\tau)}{\partial \tau}\mathrm{d}S(\mathbf{y}) + \iint_{S_\mathrm{B}} \frac{\partial \Delta p(\mathbf{y},\tau)}{\partial \tau}\mathrm{d}S(\mathbf{y})\right]_{\tau=t-\tau^*} \tag{9}$$

Based on the observation in Fig. 5 that these two source regions are highly localised at either ends of the slit, the source distribution resulting from the surface pressure integrations is now approximated by two compact sources with appropriate time delays τ^*_F and τ^*_B,

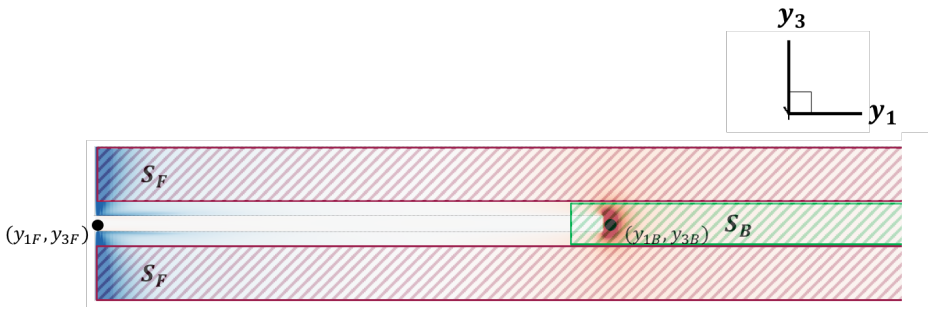

Figure 9: Illustration of front and back-edge areas. The two circles indicate the respective acoustic centres in each source region.

$$\left[\iint_{S_{\mathrm{F,B}}} \frac{\partial \Delta p(\mathbf{y},\tau)}{\partial \tau} \mathrm{d}S(\mathbf{y})\right]_{\tau=t-\tau^*} \approx \left[\dot{F}_{\mathrm{F,B}}(\tau)\right]_{\tau=t-\tau^*_{\mathrm{F,B}}} \tag{10}$$

where $[\dot{\cdot}]$ is used to denote differentiation with respect to time and where the acoustic source strengths F_F and F_B are identified as the surface integrals of the surface pressures taken over the respective acoustic regions,

$$F_{\mathrm{F}}(t) = \iint_{S_{\mathrm{F}}} \Delta p(\mathbf{y},t)\mathrm{d}S_{\mathrm{F}}(\mathbf{y}), \qquad F_{\mathrm{B}}(t) = \iint_{S_{\mathrm{B}}} \Delta p(\mathbf{y},t)\mathrm{d}S_{\mathrm{B}}(\mathbf{y}) \tag{11}$$

The time delays between the effective centres of the sources, $(y_{1\mathrm{F}}, y_{3\mathrm{F}})$ and $(y_{1\mathrm{B}}, y_{3\mathrm{B}})$ at the front and back of the slit respectively, τ^*_{F} and τ^*_{B} can be calculated from the expression for τ in Eq. (7). In this analysis we assume that the observer is located in the $x_1 - x_2$ plane at $x_3 = 0$ corresponding to the middle of the slit. For this situation, the time delays are given by,

$$\left.\begin{aligned} \tau^*_{\mathrm{F}} &= \frac{r_{\beta\mathrm{F}} - M r_{1\mathrm{F}}}{c\beta^2} \\ \tau^*_{\mathrm{B}} &= \frac{r_{\beta\mathrm{B}} - M r_{1\mathrm{B}}}{c\beta^2} \end{aligned}\right\} \tag{12}$$

where $r_1 = (x_1 - y_1)$ and $r_\beta \approx \sigma - \frac{x_1 y_1 + \beta^2 x_3 y_3}{\sigma}$, in which $y_{1\mathrm{B}} = y_{1\mathrm{F}} + h$, $y_{2\mathrm{F}} = y_{2\mathrm{B}} = 0$ and $y_{3\mathrm{F}} = y_{3\mathrm{B}} = 0$.

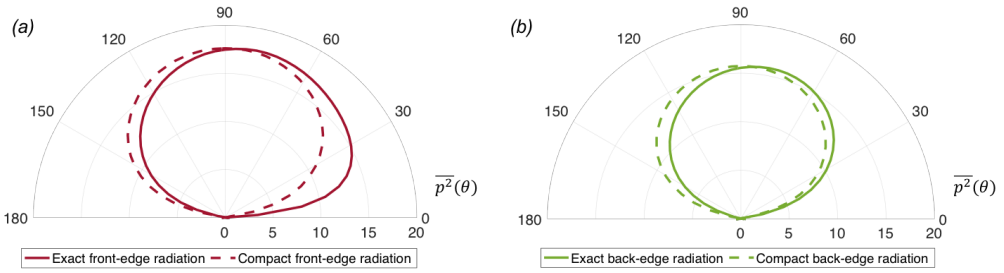

Figure 10: Comparison of the mean square pressure directivity obtained using the two-point source analytic model and the exact numerical predictions: (a) front-edge radiation - (b) back-edge radiation

In order to validate this compact source assumption the mean square pressure directivity obtained from the exact surface pressure integration of Eq. (9) is compared in figures 10(a, b) to that obtained using the compact assumption of Eq. (10) for both the front and root source regions respectively.

Figure 10 shows those mean square pressure directivities in dB in the $x_3 = 0$ plane. Figure 10(b) confirms the compact source hypothesis for the root region where very close agreement is observed between the exact and approximate directivity predictions. Similarly good agreement can also be observed for the front edge region in Fig. 10(a), except for a small range of downstream angles where significant deviations of up to 4dB between the two predictions can be observed. This front-edge source directivity is characteristic of leading edge radiation in the high frequency limit. Nevertheless, the compact source assumption appears to provide a reasonable approximation to the exact directivity over most observer angles.

Both the far field mean square pressure and its Power Spectral Density can be obtained from the auto-correlation of the far-field radiated pressure defined by Eq. (9).

$$R_{\mathrm{pp}}(\tau) = E\left[p(\mathrm{t})p(\mathrm{t}\text{-}\tau)\right] \tag{13}$$

where $E[.]$ denotes Expectation, which for turbulent flows is essentially the average taken over a sufficiently long time duration. However, since we are only dealing with a single vortex only one realisation is possible and the

Expectation is therefore redundant. Replacing the far-field radiated pressure by the expression obtained in Eq. (9), the auto-correlation of the acoustic pressure can be written in terms of the temporal derivatives of the acoustic source strengths F_{F} and F_{B},

$$R_{\mathrm{pp}}(\tau) = \left(\frac{x_2}{4\pi c\sigma^2}\right)^2 \left(E\left[\left(\dot{F}_{\mathrm{F}}(t) + \dot{F}_{\mathrm{B}}(t-\tau_{\mathrm{A}})\right)\left(\dot{F}_{\mathrm{F}}(t-\tau) + \dot{F}_{\mathrm{B}}(t-\tau-\tau_{\mathrm{A}})\right)\right]\right) \tag{14}$$

where

$$\tau_{\mathrm{A}} = \tau_{\mathrm{B}}^* - \tau_{\mathrm{F}}^* = \frac{h}{c\beta^2}(M - \frac{x_1}{\sigma}), \tag{15}$$

which represents the difference in travel times between the front and back edge sources to the observer.

Expanding Eq. (14), $R_{\mathrm{pp}}(\tau)$ can be re-written in terms of the sum of the auto-correlations of the front and back-edge sources $R_{\dot{\mathrm{F}}\dot{\mathrm{F}}}(\tau) + R_{\dot{\mathrm{B}}\dot{\mathrm{B}}}(\tau)$ plus the cross-correlation between them $R_{\dot{\mathrm{F}},\dot{\mathrm{B}}}(\tau)$, as indicated by Eq. (16).

$$R_{\mathrm{pp}}(\tau) = \left(\frac{x_2}{4\pi c\sigma^2}\right)^2 \left(R_{\dot{\mathrm{F}}\dot{\mathrm{F}}}(\tau) + R_{\dot{\mathrm{B}}\dot{\mathrm{B}}}(\tau) + R_{\dot{\mathrm{B}},\dot{\mathrm{F}}}(\tau-\tau_{\mathrm{A}}) + R_{\dot{\mathrm{F}},\dot{\mathrm{B}}}(\tau+\tau_{\mathrm{A}})\right) \tag{16}$$

Note also that for computational reasons it may be useful to use the identity $R_{\dot{\mathrm{x}},\dot{\mathrm{x}}}(\tau) = -\frac{\partial^2}{\partial\tau^2}R_{\mathrm{x,x}}(\tau)$.

4.2. Mean square pressure directivity

The mean square pressure at any point in the sound field can be calculated from Eq. (16) by setting $\tau = 0$:

$$\overline{p^2}(x_1, x_2, x_3 = 0) = R_{\mathrm{pp}}(0) = \left(\frac{x_2}{4\pi c\sigma^2}\right)^2 \left(R_{\dot{\mathrm{F}}\dot{\mathrm{F}}}(0) + R_{\dot{\mathrm{B}}\dot{\mathrm{B}}}(0) + 2R_{\dot{\mathrm{F}},\dot{\mathrm{B}}}(\tau_{\mathrm{A}})\right) \tag{17}$$

in which $\tau_{\mathrm{A}} = \tau_{\mathrm{A}}(\theta)$, where we have used the symmetry property $R_{\dot{\mathrm{B}},\dot{\mathrm{F}}}(-\tau_A) = R_{\dot{\mathrm{F}},\dot{\mathrm{B}}}(\tau_A)$.

This expression demonstrates that greatest noise reductions are obtained for the range of τ_{A} for which $R_{\dot{\mathrm{B}},\dot{\mathrm{F}}}(-\tau_{\mathrm{A}}) \leq 0$, i.e., for the range of observer angles for which the front and back-edge sources are anti-correlated. The

observer angle θ can be uniquely calculated from τ_{A} by using $x_1 = r\cos\theta$, $x_2 = r\sin\theta$, $x_3 = 0$ and $\sigma = r\sqrt{\cos^2\theta + \beta^2\sin^2\theta}$ in Eq. (12), giving:

$$\tau_{\mathrm{A}}(\theta) = \frac{h}{c\beta^2}\left(M - \frac{\cos\theta}{\sqrt{\cos^2\theta + \beta^2\sin^2\theta}}\right) \tag{18}$$

The range of possible values of τ_{A} encompassing the range of observer angles between $\theta = 0°$ (downstream) and $\theta = 180°$ (upstream) may be obtained by substituting these angle limits into Eq. (18) to give,

$$\frac{-h}{c(1+M)} \leq \tau_{\mathrm{A}} \leq \frac{h}{c(1-M)} \tag{19}$$

Eq. (18) may be inverted to give the observer angle θ for any difference in arrival time τ_{A} in the range of τ_{A} specified above,

$$\theta = \arctan\left[\frac{1}{\beta}\sqrt{\frac{1}{(M - \frac{\beta^2}{M}\frac{\tau_{\mathrm{A}}}{\tau_{\mathrm{H}}})^2} - 1}\right] \tag{20}$$

where $\beta^2 = 1 - M^2$ and τ_{H} is the time taken for the vortex to convect along the slit length h,

$$\tau_{\mathrm{H}} = h/U \tag{21}$$

Figure 11 shows the mean square pressure directivity in dB in the plane $x_3 = 0$ for the baseline case and for the slitted aerofoil obtained using the complete surface pressure integration of Eq. (8) and also using the two-source model of Eq. (9). The directivity obtained using the model can be observed to provide reasonably good agreement with the exact calculation with the greatest discrepancy of about 5dB occurring downstream of the aerofoil, consistent with the deviation observed in Fig. 10 between the exact and approximate front edge directivity functions.

Greatest noise reductions of about 8dB can be observed in the downstream direction calculated from the exact model. However, negligible noise reductions are predicted using both models in the upstream direction. This behaviour can be explained from the characteristics of the cross correlation function $R_{\dot{\mathrm{B}},\dot{\mathrm{F}}}(\tau)$ which control the directivity in Eq. (17).

Figure 12 shows the cross-correlation $R_{\dot{\mathrm{F}},\dot{\mathrm{B}}}(\tau)$ in normalised form (between -1 and 1) as the coefficient $R_{\dot{\mathrm{F}},\dot{\mathrm{B}}}(\tau)/\sqrt{(R_{\dot{\mathrm{B}},\dot{\mathrm{B}}}(0)R_{\dot{\mathrm{F}},\dot{\mathrm{F}}}(0))}$ plotted against the

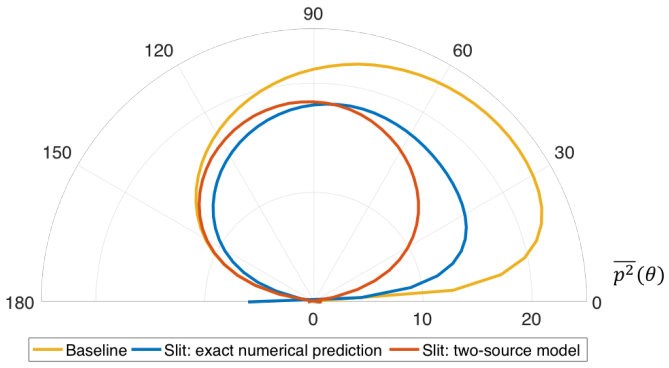

Figure 11: Directivity of the mean square pressure for both baseline and slitted aerofoil: comparison between the two-point source analytic model and the exact numerical predictions

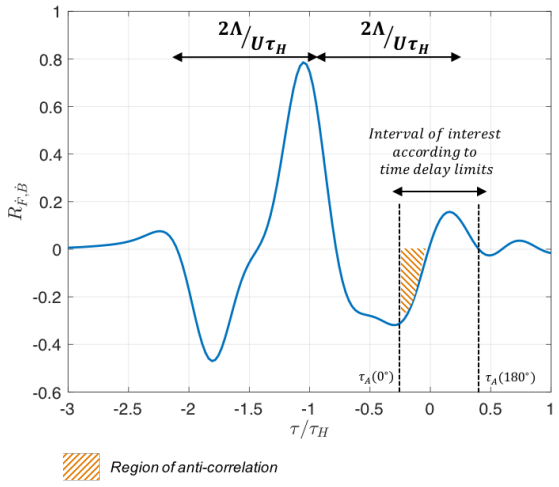

Figure 12: Cross-correlation coefficient between the front and back-edge acoustic sources

ratio τ/τ_H. Also shown in this figure is the range of possible τ_A values given by Eq. (19) ($-0.23 \leq \tau_A/\tau_H \leq 0.43$). The correlation function can be observed to peak at about 0.8 at $\tau/\tau_{\rm H} = 1.1$. Despite the presence of secondary vorticity at the back edge of the slit, the pressure fluctuations between front and back therefore remain highly correlated, which is essential for effective interference between the two source regions. Note also that the time of peak correlation, $\tau/\tau_{\rm H} = 1.1$, indicates that the effective centres of the two source regions are about 10% further apart than the physical slit height h.

The correlation function within the permissible range of $\tau_{\rm A}$ values given by Eq. (16) can be observed to be anti-correlated (as indicated by the hatched region) for $-0.23 < \tau_{\rm A}/\tau_{\rm H} < 0$ corresponding to the range of upstream angles between 0° and 73°. Greatest noise reductions in Fig. 11 are therefore obtained for this range of angles. By contrast, positive correlation is observed for $0 < \tau_{\rm A}/\tau_{\rm H} < 0.43$ corresponding to the range of predominantly downstream observer angles of 73° to 180°.

Figure 12 makes explicit that good levels of noise reduction are obtained when the range of permissible $\tau_{\rm A}$ values are situated in the anti-correlation region of the correlation function, which is mostly controlled by the vortex size Λ. To understand this behaviour more clearly the time taken for the vortex to pass over the front or back edge, $2\Lambda/U$, is indicated in Fig. 12 by horizontal arrows and can be seen to roughly match the time duration between the main peak at $\tau/\tau_{\rm H} = 1.1$ and the second largest peak at $\tau/\tau_{\rm H} = -0.2$. Noise control performance is therefore determined by the combination of the slit length and vortex size. A complete parameter study is therefore required to determine the optimum slit length for a particular vortex size corresponding to an integral length-scale for incoming turbulence.

4.3. Frequency dependence of noise reduction

The previous section has analysed the mechanism of noise reduction by a narrow leading edge slit on a flat plate interacting with a single spanwise vortex. The conditions for overall noise reduction, i.e., integrated over all frequencies, were discussed. However, this analysis provides no insight into the performance of slits across the frequency range. The two-source model developed in Section 4 is now re-formulated in the frequency domain where we derive the Power Spectral Density (PSD) of the far field pressure which is related to the mean square pressure by,

$$\overline{p^2} = R_{\mathrm{pp}}(0) = \int_{-\infty}^{\infty} S_{\mathrm{pp}}(\omega)\,\mathrm{d}\omega, \tag{22}$$

The far-field pressure PSD is related to the Fourier Transform of the autocorrelation function,

$$S_{\mathrm{pp}}(\omega) = \int_{-\infty}^{\infty} R_{\mathrm{pp}}(\tau) e^{\mathrm{i}\omega\tau}\,\mathrm{d}\tau \tag{23}$$

Substituting Eq. (16),

$$S_{\mathrm{pp}}(\omega) = \left(\frac{x_2}{4\pi c\sigma^2}\right)^2 \int_{-\infty}^{\infty} \left[R_{\dot{\mathrm{F}}\dot{\mathrm{F}}}(\tau) + R_{\dot{\mathrm{B}}\dot{\mathrm{B}}}(\tau) + R_{\dot{\mathrm{B}},\dot{\mathrm{F}}}(\tau - \tau_A) + R_{\dot{\mathrm{F}},\dot{\mathrm{B}}}(\tau + \tau_{\mathrm{A}})\right] e^{\mathrm{i}\omega\tau}\mathrm{d}\tau \tag{24}$$

Using the Fourier Transform identity $\int_{-\infty}^{\infty} R_{\mathrm{pp}}(\tau-\tau_0)e^{\mathrm{i}\omega\tau}\,\mathrm{d}\tau = S_{\mathrm{pp}}(\omega)e^{\mathrm{i}\omega\tau_0}$, Eq. (24) becomes,

$$S_{\mathrm{pp}}(\omega) = \left(\frac{x_2}{4\pi c\sigma^2}\right)^2 \left(S_{\dot{\mathrm{F}}\dot{\mathrm{F}}}(\omega) + S_{\dot{\mathrm{B}}\dot{\mathrm{B}}}(\omega) + S_{\dot{\mathrm{B}}\dot{\mathrm{F}}}(\omega)e^{\mathrm{i}\omega\tau_{\mathrm{A}}} + S_{\dot{\mathrm{F}}\dot{\mathrm{B}}}(\omega)e^{-\mathrm{i}\omega\tau_{\mathrm{A}}}\right) \tag{25}$$

Noting that the cross correlation coefficient $R_{\dot{\mathrm{B}},\dot{\mathrm{F}}}$ plotted in Fig. 12 has peak value of 0.8 shifted in time by a delay very close to τ_{H} suggests that its corresponding cross spectra $S_{\dot{\mathrm{B}},\dot{\mathrm{F}}}$ and $S_{\dot{\mathrm{F}},\dot{\mathrm{B}}}$, may be expressed in the form $S_{\dot{\mathrm{B}}\dot{\mathrm{F}}}(\omega) = |S_{\dot{\mathrm{B}}\dot{\mathrm{F}}}(\omega)|e^{\mathrm{i}\omega\tau_{\mathrm{H}}}$ and $S_{\dot{\mathrm{F}}\dot{\mathrm{B}}}(\omega) = |S_{\dot{\mathrm{F}}\dot{\mathrm{B}}}(\omega)|e^{-\mathrm{i}\omega\tau_{\mathrm{H}}}$. The phase of the cross spectrum, $\omega\tau_{\mathrm{H}}$ therefore arises entirely from the time taken for the vortex to convect along the slit.

Lastly, we may make the approximation $|S_{\dot{\mathrm{B}},\dot{\mathrm{F}}}(\omega)| = \sqrt{S_{\dot{\mathrm{F}}\dot{\mathrm{F}}}(\omega)S_{\dot{\mathrm{B}}\dot{\mathrm{B}}}(\omega)}$ owing to the high maximum correlation coefficient (≈ 0.8), the final expression for the far-field pressure PSD is given by,

$$S_{\mathrm{pp}}(\omega) = \left(\frac{x_2}{4\pi c\sigma^2}\right)^2 \left(S_{\dot{\mathrm{F}}\dot{\mathrm{F}}}(\omega) + S_{\dot{\mathrm{B}}\dot{\mathrm{B}}}(\omega) + 2\sqrt{S_{\dot{\mathrm{F}}\dot{\mathrm{F}}}(\omega)S_{\dot{\mathrm{B}}\dot{\mathrm{B}}}(\omega)}\cos(\omega(\tau_{\mathrm{A}} + \tau_{\mathrm{H}}))\right) \tag{26}$$

with $S_{\dot{\mathrm{F}}\dot{\mathrm{F}}}(\omega)$ and $S_{\dot{\mathrm{B}}\dot{\mathrm{B}}}(\omega)$ are the source strength PSD of the front and back edge respectively, calculated by taking the PSD of Eq. (11). The ratio of these frequency-dependent source strengths will be examined later

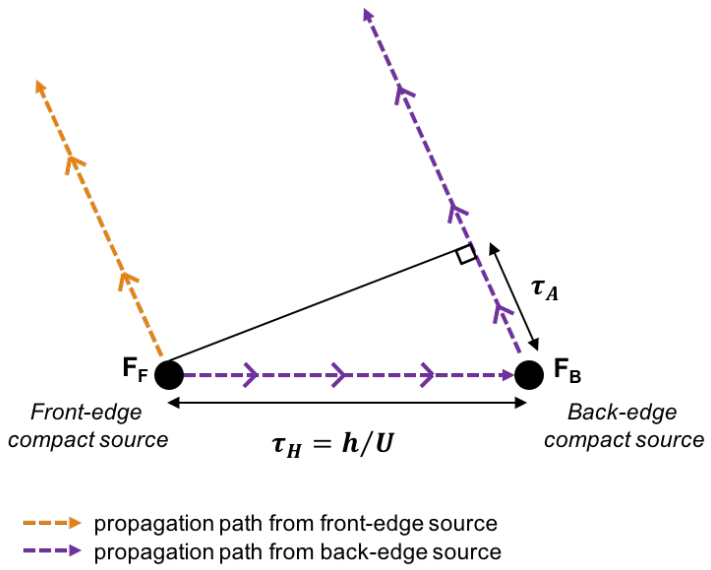

Figure 13: Illustration for the hydrodynamic and acoustic delays between the propagation from the front and back-edge sources

in subsection 4.6. Note that for computational purposes it may be useful to note the identity $S_{\dot{x}\dot{y}}(\omega) = \omega^2 S_{xy}(\omega)$.

The form of Eq. (26) for the far field pressure PSD provides a clear interpretation of the noise reduction mechanism. It demonstrates that, at any single frequency ω and observer angle θ, the front and back edge of the slit arrive with a phase difference of $\omega(\tau_H + \tau_A)$. The sum of time delays $\tau_H + \tau_A$ corresponds to the time taken τ_H for the vortex to convect from one end of the slit to the other, plus the difference in times τ_A taken for sound to propagate from the front and back edges to the far field observer, as sketched in Fig. 13.

4.4. Frequency-dependent directivity

In this section we investigate the detailed behaviour of the far field directivity as specified by Eq. (26) as a function of frequency, where τ_A is computed from θ using Eq. (20). Figure 14 shows the directivity function based on the two-source model prediction of Eq. (26) at four non-dimensional frequencies. Also shown is the directivity prediction for the slitted and base-

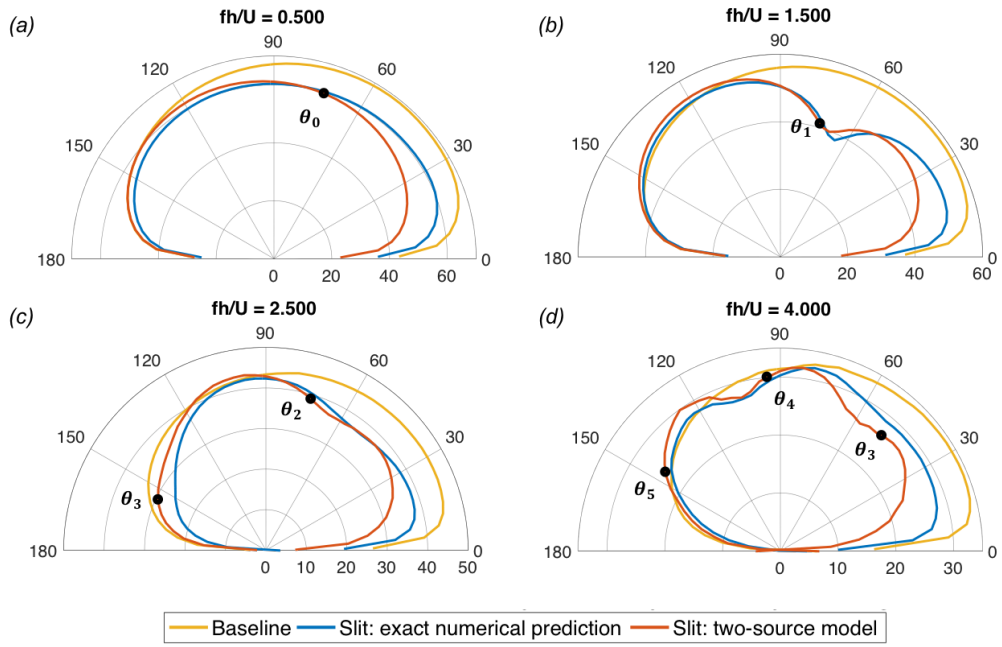

Figure 14: Far-field directivities at different non-dimensional frequencies: comparison between two-source analytic model and exact numerical predictions

line profiles obtained by taking the PSD of the exact calculation of $p(t)$ from Eq. (8).

Overall agreement between the exact and approximate far field directivity predictions can be observed to be better than 3dB over most angles, with the greatest discrepancy occurring at small downstream angles less than 20°, where differences of up to 10dB can be observed. This deviation is due to the errors in the compact approximation shown explicitly in Fig. 10(a).

The directivity functions plotted in Fig. 14, in dB in the plane $x_3 = 0$, can be observed to be highly frequency dependent. As for the mean square pressure plotted in Fig. 11, greatest noise reductions occur downstream with negligible reduction upstream at observer angles greater than about 90°. The reason for the differing upstream and downstream behaviour is because the directivity function due to the slitted flat plate is more omni-directional than for baseline directivity whose radiation pattern extends further downstream as the leading-edge source distribution becomes less compact as shown in Fig. 5. Unlike for the mean square pressure, however, the directivity pattern at a

single frequency for the slitted case can be observed to display a number of sidelobes whose number increases with increasing frequency. Clearly, therefore, in a narrow frequency band, interference between the front and back edge is important in controlling the directivity. This is in contrast with the mean square pressure directivity which is only controlled by the correlation between back and front sources.

4.5. Optimum observer position

One of the most significant features of these directivity plots is the existence of particular optimum observer angles for which the noise reductions are especially high. No such angle can be observed at the lowest frequency of $fh/U = 0.5$ plotted in Fig. 14(a). However, a single optimum angle in the directivity can be observed in Fig. 14(b) at the higher frequency of $fh/U = 1.5$, and two optimum at $fh/U = 2.5$ and $fh/U = 3.5$ in figures 14(c, d).

The presence of these optimum angles of large noise reduction corresponds to the angles θ_{n} for which the front and back edge radiate with a phase difference equal to odd multiples of 180°. The condition for these observer angles, neglecting the θ-dependence of the factor $\frac{x_2}{4\pi c\sigma^2}$, is therefore given by,

$$\omega\left(\tau_{\mathrm{H}} + \tau_{\mathrm{A}}(\theta_{\mathrm{n}})\right) = (2n+1)\pi \tag{27}$$

Substituting the expressions for $\tau_{\mathrm{H}} = h/U$ and τ_{A} from Eq. (18), the solution for θ_{n} can be expressed in terms of non-dimensional $f^* = fh/U$ as,

$$\theta_{\mathrm{n}} = \arctan\left[\frac{1}{\beta}\sqrt{\frac{1}{\left[M + \beta^2\left(\frac{1}{M} - \frac{(2n+1)}{2f^*M}\right)\right]^2} - 1}\right] \tag{28}$$

The number of distinct solutions θ_{n} to Eq. (28) can be determined from the number of n values for which the expression under the square root is positive. This condition may be shown to reduce to the number of n values for which the frequency f^* lies in the following range,

$$\frac{1}{2}(2n+1)(1-M) \leq f^* \leq \frac{1}{2}(2n+1)(1+M) \tag{29}$$

Clearly, therefore, as f^* increases there is a greater number of n values for which this condition is satisfied. There is therefore a threshold frequency

$f^*_{\min}$ below which no optimum observer angle exists. This frequency, $f^*_{\min}$ is associated with the lower limit of Eq. (29) for $n = 0$,

$$f^*_{\min} = \frac{1}{2}(1 - M) \tag{30}$$

From the expression for θ of Eq. (28), the minimum frequency $f^*_{\min}$ can be seen to correspond to $\theta = 0°$. As the frequency is increased, Eq. (28) suggests that this angle of maximum noise reduction travels from 0° to 180°, corresponding to the upper limit of Eq. (29) of $f^* = (1 + M)/2$. As the frequency f^* is increased, there is a larger number of optimum angles that can co-exist at the same frequency. This behaviour is consistent with the directivity plots in Fig. 14 where the different solutions are marked as circles. Note the small shift between the predicted and the exact optimum angles, due to the omission of the factor $\frac{x_2}{4\pi c\sigma^2}$ in the estimate of $\theta_{\rm n}$ given by Eq. (28).

4.6. Source balance on slitted aerofoils

According to the simple two-source model of Eq. (26), the noise radiation from the slitted serration is determined by the two source strengths $S_{\dot{F}\dot{F}}(\omega)$ and $S_{\dot{B}\dot{B}}(\omega)$ at the front and back of the slit. Greatest noise reductions are achieved when these source strengths are equal. We now examine the balance of these source strength as a function of frequency.

Figure 15(a) shows the variation in the source strengths $S_{\dot{\rm F}\dot{\rm F}}(\omega)/\Phi_{\rm vv}(\omega)$ and $S_{\dot{\rm B}\dot{\rm B}}(\omega)/\Phi_{\rm vv}(\omega)$ expressed in dB, versus f^*, where $\Phi_{\rm vv}(\omega)$ is the velocity spectrum of the incoming vortex, plotted in Fig. 3(b). This normalisation is necessary to remove the oscillations in the noise spectrum due to those in the velocity spectrum to allow the pressure response on the surface of slitted serration to be more clearly identified. Also shown is the corresponding integrated source strength of the baseline aerofoil normalised on $\Phi_{\rm vv}(\omega)$, which may be a misleading indicator of source strength since it is no longer compact in this sharp edge case (see Fig. 5) but may provide a useful means with which to compare the source strengths.

The source strength spectra due to the baseline flat plate and the front edge of the slit after normalisation by the highly oscillatory velocity spectrum in Fig. 3(b), can be observed to vary smoothly and by less than 12dB over the frequency range. The absence of oscillations in these spectra suggests that these source strengths are closely linked to the incoming velocity spectrum. However, the pressure response due to different vortex dimensions

must be calculated to establish whether there is a linear association between the pressure and velocity spectra for this complex slitted geometry. The source spectrum due to the baseline case can be observed to decay very slowly with increasing frequency, consistent with the classical frequency dependence of leading edge interaction noise. The integrated source strength at the front the slit can be seen to generally increase with increasing frequency but never exceeds the baseline source strength. However, the frequency spectrum at the back of the slit, after normalisation by the incoming velocity spectrum, can be observed to exhibit much larger variations with frequency. Sharp peaks in the spectrum can be observed, which coincide with the dips in the velocity spectrum plotted in Fig. 3(b). Clearly, therefore, the source spectrum at the back of the slit is not directly related to the incoming velocity spectrum, which is consistent with the presence of strong secondary vorticity.

For this particular choice of slit dimensions (h and w) and choice of vortex size, the front and back edge source strengths can be observed to closely match at $f^* = 1.5$. Maximum levels of noise reduction are therefore predicted at this frequency, as shown in the directivity plot of Fig. 14(b), where sound pressure level reductions of up to 20dB are shown at the optimum angle θ_1, where the total phase delay $\omega(\tau_A + \tau_H)$ equals 3π. At the frequency of $f^* = 0.5$, however, the source strengths can be seen to differ by about 8dB, suggesting relatively weak interference effects at this frequency. This prediction is consistent with the directivity plot of Fig. 14(a) at $f^* = 0.5$ in which poorer levels of noise reduction of around 10dB are observed and entirely attributed to a direct reduction in source strengths on the plate compared to the baseline case.

It is clear, therefore, that achieving the desired equality between the source strengths at the front and back of the slits is not straightforward. However, further work is needed to determine the exact dependence of these source strengths to the slit dimensions.

4.7. Sound power reduction

In this final section we investigate the total sound power reduction due to the slit compared to the baseline case. The radiated sound power per unit aerofoil span can be be estimated by assuming that the aerofoil, whose span is infinitely long, radiates to the far field as a cylindrical wave with negligible spanwise variations in radiated pressure,

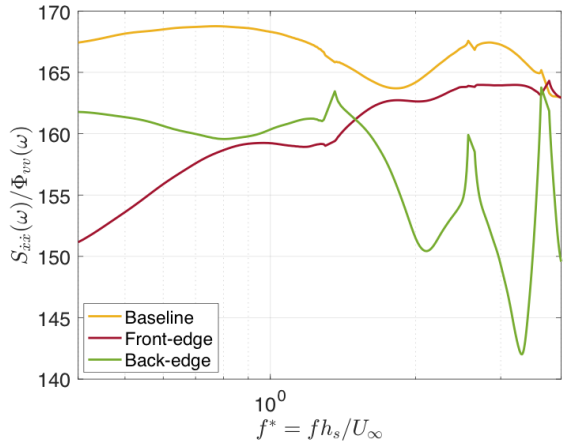

Figure 15: Source strengths on the aerofoil surface for the baseline case and for the slitted case at the front and back-edge regions

$$P(\omega) = \int_0^{2\pi} I_r(r, \theta, \omega)\, r \mathrm{d}\theta \tag{31}$$

where $I_\mathrm{r}(r, \theta, \omega)$ is the radial component of acoustic intensity transmitted in a uniform mean flow with Mach number M. Following Blandeau ([22]) $I_\mathrm{r}(r, \theta, \omega)$ may be determined from the mean square pressure spectrum and the non-dimensional factor $F(\theta, M)$,

$$I_\mathrm{r}(r, \theta, \omega) = \frac{S_\mathrm{pp}(r, \omega, \theta)}{\rho c} F(\theta, M) \tag{32}$$

with,

$$F(\theta, M) = \frac{\beta^4 \sqrt{1 - M^2 \sin^2\theta}}{\left(\sqrt{1 - M^2 \sin^2\theta} - M\cos\theta\right)^2} \tag{33}$$

The predicted sound power reduction is shown in Fig. 16 using both the exact surface pressure integration and the radiated pressure obtained from the two-source model.

Agreement between the exact calculation of sound power reduction and that obtained using the simple two-source model are within 2dB over the

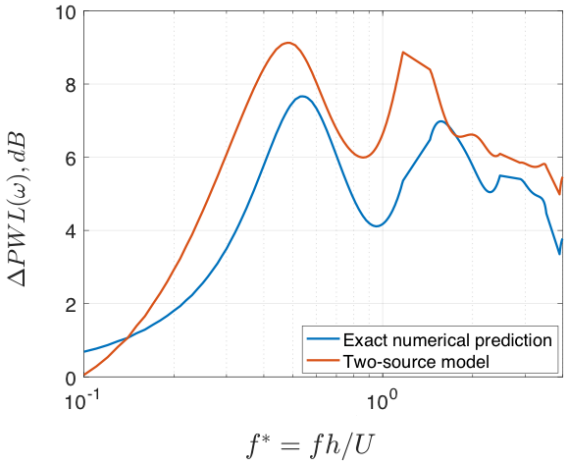

Figure 16: Sound power predictions for the baseline case and slitted aerofoil, comparing the exact numerical prediction with the two-source model

entire frequency range, thereby supporting the validity of the two source model. Consistent with measurement plotted in Fig. 1, negligible noise reductions are predicted in the low frequency limit but increase as frequency increases. Also consistent with the measurements are the peak frequencies of maximum sound power reductions very close to the theoretical frequencies of $f^* = 0.5, 1.5 and 2.5$, with maximum reductions at $f^* = 1.5$ of 9dB. Even though the detailed pressure directivity functions are complicated functions of frequency and observer angles, Fig. 14, after integration over θ, the total sound power reductions are greatest at $f^* = f\tau_H = (2n+1)/2$. At higher frequencies, however, predicted sound power reductions diminish due to the increasingly large differences between the source strengths at the front and back edges, as shown in Fig. 15.

4.8. Two-source model results for other slit configurations

In this section, we investigate the validity of the two-source model for different combinations of slit lengths and slit widths. The exact numerical procedure described in Section 4 was repeated for four other slit configurations comprising $(h/2, w)$,$(2h, w)$,$(h, w/2)$ and $(h, 2w)$, where (h, w) corresponds to the original case considered in Sections 3 and 4. Figure 17 a) shows the sound power reduction spectra for the different cases plotted

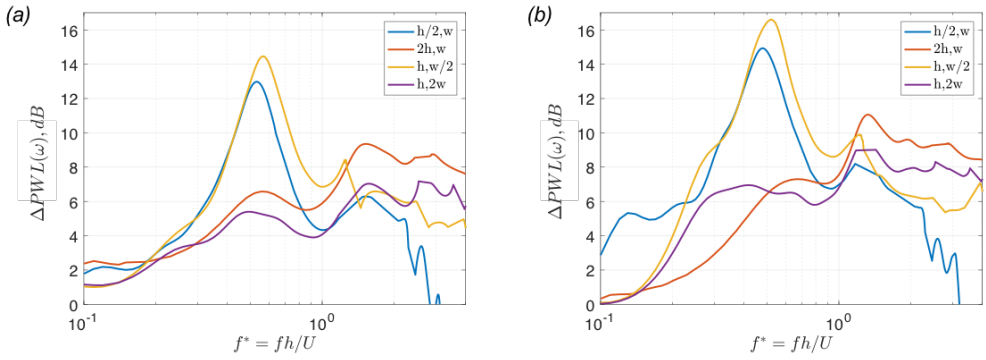

Figure 17: Sound power predictions for the baseline case and slitted aerofoil, comparing the exact numerical prediction with the two-source model for different slit configurations

against $f^* = fh/U$, computed exactly using Eq. 8, while Figure 17 b) is the corresponding sound power reduction spectra obtained using the two-source model. The two-source model predictions can be observed to provide reasonable agreement with the exact calculation in all four cases, thereby validating the noise reduction mechanism proposed in this paper. Of the four cases, the case $(h, w/2)$ gives the largest maximum noise reduction of 14.3dB at $f^* = 0.5$ and the best overall noise reduction of 7dB. Clearly therefore, the noise reduction performance of the slit is highly sensitive to slit length and slit width. A complete parametric study is therefore required to identify the optimum slit parameters.

5. Conclusion

The mechanism and performance of slitted leading edge serrations for reducing turbulence - aerofoil interaction noise has been investigated in detail from numerical solutions of the Euler equations. These predictions have confirmed the hypothesis of Chaitanya [14] that the essential noise reduction mechanisms are related to an overall reduction in source strength and through the interference between two sources at either ends of the slit. This paper has shown that the initial prescribed vortex impinging on the plate generates two sources at either end of the slits, whose levels are affected by secondary streamwise vortices originated at the slit corners and interacting with the front and back-edges of the slit.

The simple two-source model proposed by Chaitanya [14] for the sound power reductions has been extended to include predictions of the pressure directivity. Reasonable agreement between this simple model and the exact calculations have been obtained. The existence of optimum observer angles at each frequency has been identified at which maximum noise reductions are observed. Overall noise reductions integrated over all frequencies has been shown to be related to the degree of anti-correlation between the front and back edge of the slit. This paper has confirmed that leading edge slits are a promising technology for reducing broadband interaction noise that requires a much smaller modification to the leading edge than conventional serrations in terms of the aerofoil area modification. However, their relative effects on aerodynamic performance and structural integrity remain to be determined.

Acknowledgments

This work was supported by the EPSRC (Engineering and Physical Sciences Research Council). Rolls-Royce Plc is also acknowledged for the financial and technical support given, along with the University of Southampton for the support regarding the local supercomputing facility IRIDIS4.

References

[1] P. Chaitanya, Aerofoil geometry effects on turbulence interaction noise, Ph.D. thesis, University of Southampton, UK (2017).

[2] B. Lyu, M. Azarpeyvand, On the noise prediction for serrated leading edges., Journal of Fluid Mechanics 826 (2017) 205–234.

[3] M. Roger, C. Schram, L. D. D. Santana, Reduction of airfoil turbulence-impingement noise by means of leading-edge serrations and/or porous material., 19th AIAA/CEAS Aeroacoustics Conference, Berlin, Germany 2013-2108 (2013).

[4] L. Ayton, P. Chaitanya, Analytic solutions for reduced leading-edge noise aerofoils., 24th AIAA/CEAS Aeroacoustics Conference, Atlanta, Georgia, USA 2018-3284 (2018).

[5] V. Clair, C. Polacsek, T. L. Garrec, G. Reboul, Experimental and numerical investigation of turbulence-airfoil noise reduction using wavy edges., AIAA Journal 51 (2013) 2695–2713.

[6] A. Lau, S. Haeri, J. W. Kim, The effect of wavy leading edges on aerofoil gust interaction noise., Journal of Sound and Vibrations 332 (2013) 6234–6253.

[7] J. W. Kim, S. Haeri, P. Joseph, On the reduction of aerofoil-turbulence interaction noise associated with wavy leading edges., Journal of Fluid Mechanics 792 (2016) 526–552.

[8] J. Turner, J. W. Kim, Aeroacoustic source mechanisms of a wavy leading edge undergoing vortical disturbances., Journal of Fluid Mechanics 811 (2017) 582–611.

[9] F. Gea-Aguilera, J. Gill, D. Angland, X. Zhang, Wavy leading edge airfoils interacting with anisotropic turbulence., 23rd AIAA/CEAS Aeroacoustics Conference,Denver, Colorado 2017-3370 (2017).

[10] S. Narayanan, P. Chaitanya, S. Haeri, P. Joseph, J. W. Kim, C. Polacsek, Airfoil noise reductions through leading edge serrations., Physics of Fluid 27 (2015).

[11] T. P. Chong, A. Vathylakis, A. McEwen, F. Kemsley, C. Muhammad, S. Siddiqi, Aeroacoustic and aerodynamic performances of an aerofoil subjected to sinusoidal leading edges., 21st AIAA/CEAS Aeroacoustics Conference, Dallas, TX, USA 2015-2200 (2015).

[12] P. Chaitanya, S. Narayanan, P. Joseph, C. Vanderwel, J. Turner, J. W. Kim, B. Ganapathisubramani, Performance and mechanism of sinusoidal leading edge serrations for the reduction of turbulence aerofoil interaction noise., Journal of Fluid Mechanics 818 (2017) 435–464.

[13] P. Chaitanya, S. Narayanan, P. Joseph, J. W. Kim, Leading edge serration geometries for significantly enhanced leading edge noise reductions., 22nd AIAA/CEAS Aeroacoustics Conference, Lyon, France 2016-2736 (2016).

[14] P. Chaitanya, P. Joseph, Slitted leading edge profiles for the reduction of turbulence-aerofoil interaction noise., The Journal of the Acoustical Society of America 143 (2018) 3494–3504.

[15] P. Chaitanya, P. Joseph, L. J. Ayton, Leading-edge profiles for the reduction of airfoil interaction noise, AIAA Journal (2019).

[16] M. Cannard, P. Joseph, J. W. Kim, P. Chaitanya, Numerical investigation into slitted leading-edge profiles for reducing interaction noise., 25th International Congress on Sound and Vibration 2018, Hiroshima, Japan 3 (2018) 1366–1373.

[17] J. W. Kim, An advanced synthetic eddy method for the computation of aerofoil turbulence interaction noise, Journal of Computational Physics 287 (2015) 1–17.

[18] J. W. Kim, Optimised boundary compact finite difference schemes for computational aeroacoustics., Journal of Computational Physics 225 (2007) 995–1019.

[19] J. W. Kim, High-order compact filters with variable cut-off wavenumber and stable boundary treatment., Computers and Fluids 39 (2010) 1168–1182.

[20] R. Amiet, Acoustic radiation from an airfoil in a turbulent stream., Journal of Sound and Vibration 41 (1975) 407–420.

[21] M. Goldstein, Aeroacoustics, NASA SP, Scientific and Technical Information Office, National Aeronautics and Space Administration, 1974.

[22] V. Blandeau, P. Joseph, G. Jenkins, C. Powles, Comparison of sound power radiation from isolated airfoils and cascades in a turbulent flow., The Journal of the Acoustical Society of America 129 (2011) 3521–3530.

LaTeX Source Files and Figures

Click here to download LaTeX Source Files: JSV_2019_Cannard_Revision.zip

Rebuttal letter to the reviewers' comments on the paper JSV-D-19-01748
By
Marine Cannard, Phillip Joseph, Jacob Turner, Paruchuri Chaitanya and Jae Wook Kim

We would like to take this opportunity to thank the reviewers for taking the time to review our paper and for his or hers generally constructive comments. We have been careful to address each comment, which we present below.

All page and line numbers refer to the initial manuscript

1. Reviewer's comment

Page 1 line 53 - "between turbulent flow and the aerofoil leading edge"

Authors' response: Thank you. We now have changed this sentence to:
1,53. "occurs through the interaction between turbulent flow and the aerofoil leading-edge"

2. Reviewer's comment

Page 2 line 33 - define U.

Authors' response: Now defined on line XX, which now says**:**
2, 33. "where U is the mean flow speed"

3. Reviewer's comment

Page 2 line 52 - the slitted profile shows better noise reductions seemingly only at low frequencies.

Authors' response: We agree with this comment. We have now modified this sentence to say,

"….. significantly better noise reductions than the conventional profile at low frequencies while generally providing smaller noise reductions at high frequencies due to trailing edge interaction [15])".

We have included a reference to a new paper [15] which shows the poorer performance of slits compared to other serrations at high frequencies. However, we note that slits still provide the best overall noise level reductions.

4. Reviewer's comment

Page 2 line 54 - "these peaks can only be explained..." Why only this way?

Authors' response: We have now modified this sentence to say,

"…… fh/U~ 0.5, 1.5 and 2.5. This condition implies a phase difference between two compact sources at either ends of the slit of p, 3p and 5p. The most likely interpretation of this finding therefore is that the peaks are the result of destructive interference between these two sources". This hypothesis will be confirmed in the numerical surface pressure predictions presented below."

5. Reviewer's comment

Page 3 line 54 - "upstream of the aerofoil"

Authors' response: Now corrected

6. Reviewer's comment

Page 5 line 50 - how do you know the spanwise effects will be less significant? How also do you know the effects of off-centering the vortex (vortex center line above or below plate) will not have a significant effect on your conclusions.

Authors' response

The reviewer makes some valid comments about the representation of the problem in our paper. It is true that we cannot be certain that spanwise turbulence effects and 'off-centreing' the vortex from the leading edge on the acoustic response of the slit will be insignificant. We are encouraged by the good qualitative agreement the numerical predictions of sound power reduction given in the paper in section 4.7 and the measured reductions on a flat plate *and* a realistic aerofoil reproduced in figure 1 of the paper. However, we accept that this effects will have some influence on the absolute noise reductions. We emphasise that our intention is to understand the fundamental noise reduction mechanisms and not to provide detailed predictions of noise reduction performance.

7. Reviewer's comment

Page 6 line 49 - why is only one case considered? Surely to draw useful conclusions you must test other cases of slit aspect ratios. Does the specific length of the slit affect the properties of the induced vorticity and if so, can the slit still be deemed better than the sinusoid?

Authors' response

We agree that our paper would be enhanced by the inclusion of some additional cases. We were reluctant to add additional material as the paper is already quite lengthy. We now include four cases additional to the baseline case (h,w) of (2h,w), (h/2,w), (h,2w) and (h,w/2). A new figure 17 is now

given comparing the predicted sound power level spectra, together with the predictions obtained from the two-source model.

We now add a new sub-section in the paper, “Two-source model results for other slit configurations” In this new section we state that

“The two-source model predictions can be observed to provide reasonable agreement with the exact calculation in all four cases, thereby validating the noise reduction mechanism proposed in this paper. Of the four cases, the case (h,w/2) gives the largest maximum noise reduction of 14.3 dB at f^* = 0.5 and the best overall noise reduction of 7 dB. Clearly therefore, the noise reduction performance of the slit is highly sensitive to slit length and slit width.”

8. Reviewer’s comment

Page 7 line 37 - If viscous effects are neglected, does the vortex not simply stretch around the edge of the airfoil? How is it ’cut’ by the plate without viscosity?

The reviewer is correct that for an inviscid (vortex filament) model, there is a singularity at the core. A vortex filament cannot end abruptly in the flow, and therefore cannot be cut into two separate vortices. However, in our case, although we consider an inviscid simulation (Euler equations), the vortex is modelled with a finite core region and therefore a viscous vortex model is used. The terminology of cutting vortex in an inviscid simulation is also used in other papers, as in "High-resolutions simulations of parallel blade-vortex interactions" by Thom & Al (2010), AIAA Journal Vol. 48, No.10

9. Reviewer’s comment

Page 8 line 27 - rhs should be RHS.

Authors’ response: Corrected

10. Reviewer’s comment

Page 8 line 27 - “equations in and represents” needs correcting.

Authors’ response: Equation number now inserted.

11. Reviewer’s comment

Page 10 line 27 - σ has been used previously to define the vortex size. Please use a different symbol.

Authors’ response: Symbol for vortex size now changed to σ_{vortex}

12. Reviewer's comment

Page 11 line 20 - the discussion of the front edge of the vortex interacting with the back of the slit while simultaneously the back edge of the vortex interacts with the front of the slit must be a particular case due to the parameters chosen. For any other flow speed, height of vortex centerline, or slit type this would not happen simultaneously. How therefore can this be intrinsic to your conclusions? Practically speaking one would not be able to design the perfect slit as you have used, so you should not restrict to just this case.

Authors' response

We accept that issue is not as clear as it should be in the paper. The explanation for this is rather subtle. We emphasise that it is NOT necessary for the front and back edges to interact with the vortex simultaneously for destructive interference to occur. Destructive interference will always occur. The additional cases which include one example where the slit length is greater than the eddy size, show that interference is still present, confirmed by the existence of the peaks at $fh/U = 0.5$, 1.5, 2.5 …

13. Reviewer's comment

Page 13 line 18 - "flate" to "flat"

Authors' response: Now corrected

14. Reviewer's comment

Page 13 line 23 - in this section you discuss vortices generated by the slit sides and their impingement on the back of the slit. How would this alter in a loaded configuration? Would the side vortices still interact with the back of the slit or would they pass over the surface?

Authors' response

The reviewer raises an interesting and valid question for which we cannot be absolutely certain as no simulations were possible for realistic loaded aerofoils. However, after further analysis of our numerical data we come to the new conclusion that the side vortices generated at the front edge do not need to reach the back edge of the slit for the back edge source to be generated. Indeed the front and back edge sources are mostly generated by the main (incident) vortex but whose level is affected by the side vortex. Even if the side vortex doesn't reach the back edge, as might be the case in a loaded aerofoil, a back edge source is still generated by the main vortex which also generated secondary vorticity directly at the back edge. The fundamental noise generation mechanism therefore remains unchanged.

15. Reviewer's comment

Page 15 line 36 - the two-source model seems to rely on numerically determining the surface pressure, is this correct? If so, I question how useful this is in determining noise reduction as surely

you cannot know the source strengths and their variation will significantly impact results.
Additionally,
I raise again the point of it being pertinent you include a second test case. How are you sure the two-source model remains accurate for different slits and different frequencies?

Authors' response

The reviewer is correct in his or her explanation of how the two source model is implemented and his or her assertion that we cannot know the source strengths. However, we wish to emphasise that the purpose of the model is to assist in the *understanding* of the noise generation mechanism and *not* to provide a method for predicting noise reductions.

We hope that the inclusion of four additional cases will reassure the reviewer of the validity of the two source model interpretation.

As explained in Qu. 7 new cases have now been added and analysed.

16. Reviewer's comment

Fig 10a and Fig 11 - The exact solution line along the 180 degrees angle seems suspicious. Please check.

Authors' response

Thank you. The reason for this strange behaviour at these limiting angle is because the sound Pressure Level values have become negative. This is because our SPL values are defined relative to some arbitrary reference pressure as only the relative differences are of interest in this paper. Absolute values of not of interest here since the choice of vortex strength is arbitrary. Our choice of reference pressure was chosen to ensure that the SPL varied between 0 and 20dB. These have now been replotted to remove this anomaly.

17. Reviewer's comment

Page 18 equation 13 - typesetting is likely incorrect.

Authors' response: Oops. Now corrected, thank you.

18. Reviewer's comment

Fig 14 - The discussion on page 27 does not seem to correlate with the positions of the _ spots on the plot. Should these spots be where there is maximum reduction? That does not appear the case.

Authors' response

The reviewer is correct. There is a slight deviation from the predicted values shown as spots and the actual minima. We already explain this in the text on page 27 line 14. In deriving Eq. (28) for the radiation minimum we neglect the $x_2/4\pi c\sigma^2$ term and hence our prediction is only an approximation. This approximation is explained again at the end of the section 4.5.

Rebuttal letter to the reviewers' comments on the paper JSV-D-19-01748
By
Marine Cannard, Phillip Joseph, Paruchuri Chaitanya and Jae Wook Kim

We would like to take this opportunity to express our sincere appreciation to this reviewer for taking the considerable time to review our paper and for his or hers generally constructive comments. He or she has found some significant inconsistencies that we hadn't detected. We have been careful to address each comment, which we present below. Line numbers refer to the initial first paper draft.

All page and line numbers refer to the initial manuscript

1. Reviewer's comment

p. 2, ll. 32-34: "Clearly, the slitted profile... the conventional profile." Yes, up to $fh/U = 1.5$, but less so at higher frequencies. Is the high frequency behaviour related to what is discussed in section 4.7? Or could there also be an effect of another source, not affected by the slits, like trailing edge noise dominating the radiation at these frequencies?

Authors' response

We agree that this issue is not well explained in the paper. The poorer behaviour at high frequencies compared to conventional profiles is mostly unrelated to the source strength balance issue discussed in section 4.7. The reason for poorer behaviour at high frequencies we believe is due to the secondary vortex passing over the trailing edge which generates an additional source which then masks the noise reductions at high frequencies. The different behaviours of different leading edge geometries are shown in a recent experimental paper by Chaitanya who shows that while the slits provide best noise reductions at low frequencies $fh/U < 1.5$, and best noise reduction overall, they are slightly inferior at higher frequencies.

We have now modified the paper to indicate that superior reductions are only achieved at $fh/U < 1.5$. Thus, we now say on page 2 line 49

"….. significantly better noise reductions than the conventional profile at low frequencies while generally providing smaller noise reductions at high frequencies due to trailing edge interaction [15]".

We have included a reference to a new paper [15] by Chaitanya which shows the poorer performance of slits compared to other serrations at high frequencies. However, we note that slits still provide the best overall noise level reductions.

2. Reviewer's comment

p. 4, ll. 15-16: "... injected upstream of the plate through the use of a sponge layer." Since the vortex is introduced only at $t = 0$, is it necessary to use a sponge layer? Couldn't it just be imposed as an initial field?

Authors' response

In principle the reviewer is correct. However, we note that the sponge layer is also used to force the flow to the potential mean flow condition. Moreover, the sponge layer also absorbs any residual reflections at the boundaries.

3. Reviewer's comment

p. 6, ll. 7-9: "Furthermore, ... than the turbulence length scale." I understand that you can investigate the reduction mechanism of a slit with a 2-D vortex. What about the relationship between the turbulence length scale and the "wavelength" λ? Was λ chosen based on previous experimental work [14] as the value providing the best reduction in this previous work?

Authors' response

Our intention with this paper is to focus in detail on the vortex dynamics, surface pressure fluctuations and the far field radiation due to a single slit interacting with a single spanwise vortex. The significant difference between the slit and most other geometries considered in [14] is that the slit is narrow and the response is highly localised to the front and back of the slit. We anticipate that spanwise coherence effects arising from 3D turbulence will be of less importance in the case of the slit compared to, for example, the single wavelength serration. With the use of a spanwise vortex and periodic boundary conditions, the radiation from adjacent slits are perfectly coherent. However, in practice adjacent slits are likely to be largely incoherent when the length-scale is greater than the wavelength λ. However, in both cases we strongly believe that the essential noise reduction mechanism is identical.

4. Reviewer's comment

p. 6, ll. 16-18: "As the vortex convects... during the upwards stroke." In this sentence, are the positive and negative pressure references for the upper side of the plate? Since the radiation is dipolar, the pressure on the lower side is of opposite sign. Or are you referring to the pressure jump $p_{upper} - p_{lower}$?

Authors' response

Thank you. We appreciate the confusion. In section p. 6, ll. 16-18 we refer to the pressure on the upper side (in response to the upwash and downwash). However, subsequent references to the 'surface pressure' refer to the pressure difference (jump).

We now add on page 6 line 28,
"…….. positive pressure is generated during the downward stroke *on the upper side of the* plate with the opposite behaviour occurring on the lower side"

5. Reviewer's comment

p. 6, l. 26: "The leading edge is therefore assumed... from the vortex centre."
Just to avoid any confusion, you can specify that this is the initial position of the vortex.

Authors' response

Thank you. To make this clearer we now add the additional sentence,
"… the leading edge of the vortex is therefore assumed to be located at Λ from the vortex centre which is the initial position of the vortex, referred to as x_0 in Eq. (3)".

6. Reviewer's comment

p. 8, l. 1: e_t refers to the total energy and not the internal energy. Also, there is a typo in the definition. I believe it should be et = $p/\rho(\gamma-1) + (u_j u_j)/2$

Authors' response: Thank you. There was a typo in this equation with the bracket ']' in the wrong place. The equation refers to total energy and this is now made clear in the paper.

7. Reviewer's comment

p. 8, ll. 16-17: "The use of a multi-block grid... in the complete domain..." It is not completely clear to me what is meant there.

Authors' response

We are a bit unclear about the source of confusion in this sentence. However, we have modified the sentence to enhance clarity. We now say,
"the use of a multi-block grid facilitates the meshing of complex regions and introduces greater efficiency in running the code in parallel"

8. Reviewer's comment

p. 9 l. 14: "... the prediction obtained from Amiet's model..." To make this prediction using Amiet's model, did you only account for the first leading edge contribution in the iterative process (since you work with an infinite chord)? It might be interesting to specify it for readers.

Authors' response

The reviewer is correct to suggest that there is no trailing edge correction applied to the prediction. To make this clear, we now add on page 9 line 46
"Note that, since the aerofoil is chord is essentially infinitely long no trailing edge correction was applied".

9. Reviewer's comment

Maybe it could be useful to provide a reference for the expressions of the dipole radiation with the far-field observer hypothesis, if you have one (from a book?). The definition of $\beta^2 = 1 - M^2$ should be given after eq. (7). The symbol σ is also used earlier in the paper in the definition of the vortex. This might be confusing.

Authors' response

The term $\beta^2 = 1 - M^2$ is now defined on line page 10 line 24 and the reference to the book "Aeroacoustics" by Goldstein (section 3,2) is now included to provide the derivation of the Green's function solution.

10. Reviewer's comment

p. 11: The use of the terms "leading edge" and "trailing edge" for the vortex might be a bit confusing.

Authors' response

Please note that in the paper we refer only refer to the front edge of the flat plate to avoid confusion with the leading edge of the vortex. Please also note that we also refer to figure 5b, which provides a schematic of the vortex leading edge interacting with the back edge of the slit. We hope that together the meaning of 'vortex leading edge" is clear.

11. Reviewer's comment

Section 3.1: I think that in addition to the contour plots of Fig. 5, it might be useful to show pressure jump profiles at the different times for the baseline and slitted plates (with a profile going through the middle of the slit and another between two slits).

Authors' response

We have computed the time variation of pressure jump at five positions between the slit corner and furthest from the boundary (i.e, further from the slit). The results are shown below. We do not believe that adding this figures provides any new insight into the noise reduction mechanism and therefore have no included it into the paper. However, we are prepared to add it to the paper if the reviewer thinks that this is a useful result.

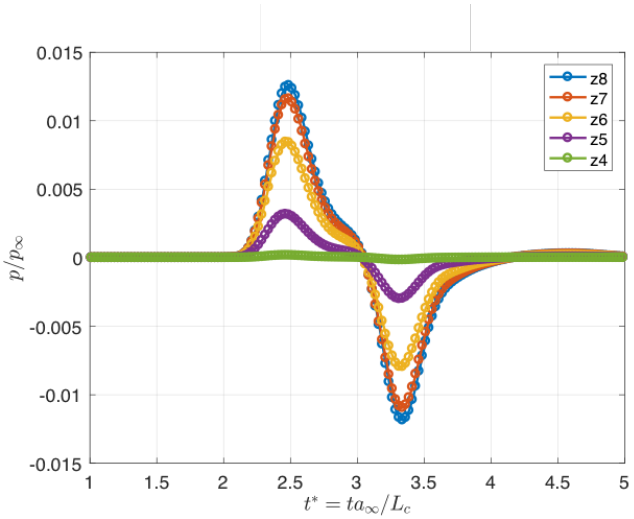

Figure 1:Time variation of pressure jump at five positions between the slit corner and furthest from the boundary (i.e, further from the slit)

12. Reviewer's comment

section 3.2.1: I am not sure that I understand that part. From what I read in [8], especially in section 3.2 and Fig. 14, the spanwise vorticity w_z generated during the impact of the vortex exists both for the baseline and serrated case. It also seems to be more important for the baseline case than for the serrated aerofoils in [8].

Authors' response

We agree that secondary spanwise vorticity is more important for the baseline and serrated leading edges as shown in Figure 14b in reference 8 since the discontinuity is purely in the streamwise direction while there is smaller discontinuity in the with streamwise and spanwise directions in the case of the wavy serration. To make this clearer, we now add on page 13 line 19:

"….. as it is also the case for a straight leading edge airfoil …."

13. Reviewer's comment

p. 13, l. 11: "streamwise velocity discontinuity ($\delta x/\delta x_3 > 0$)". Do you mean normal velocity discontinuity?

Authors' response

We mean discontinuity of the streamwise velocity in the spanwise direction x_3. To make this clearer, we now add on page 13 line 27:

"….. in the spanwise direction….."

14. Reviewer's comment

p. 15, ll. 1-3: "The comparison between...than at the front" I agree that the vorticities are higher at the back edge than at the front for most of the span. But we can notice that as we get close to the corner of the slit at the font edge (Fig. 8(a)), w_x reach values of the same order of magnitude than those of Fig. 8(b).

Authors' response

Thank you. We now make this clearer. We now add on page 15 line 27:

"most of the span *except close to the front corner where the streamwise vorticity is generated and therefore reaches comparable levels to the levels at the back*."

15. Reviewer's comment

Section 3.2: just as a general remark on that section, the use of sub-sub-sections leads to short or very short paragraphs (see section 3.2.1). I am not sure that all these subdivisions are needed.

Authors' response

We have looked careful again at the structure of the paper. We believe that the present structure of smaller sections aids clarity. We hope that the reviewer finds this acceptable.

16. Reviewer's comment

Eq. (10): the meaning of [˙] should be defined after this equation. Currently, it is defined after eq. (15).

Authors' response

The definition of [.] was given after Eq. (15) but is moved to after equation (10) to make this clearer.

17. Reviewer's comment

Figure 10: Could you specify the positions of the observers (*r, x*3 = 0). Also, could you indicate that the results are in dB.

Authors' response

We now specify that the mean square pressure directivity is in the *x*3 = 0 plane, plotted in dB.

We now add the additional sentence,
"Figure 10a and b shows those mean square pressure directives in dB in the x3 = 0 plane".

18. Reviewer's comment

Eq. (13): I believe there is a typo in the LaTeX code of this equation.

Authors' response: Thank you. Now corrected.

19. Reviewer's comment

p. 18, l. 14-16: "However, since... and the Expectation is therefore redundant."
I am not entirely sure to understand what you are meaning here. I understand that your signals for a single vortex have a finite support in time and that you realisation for a single vortex is deterministic. But could you please specify how you calculate R_{pp} in practice? Is it something like: $R_{pp} = \int_{-\infty}^{\infty} p(t)p(t-\tau)dt?$ But since your signals have a finite time support of duration T, corresponding to the time needed for the vortex to cross the computational domain, you only integrate between 0 and *T*?

Authors' response

The reviewer is absolutely correct in his or her's interpretation of our analysis. The 'correlation' is only evaluated over the short duration for which the vortex passes over the slit. The integral expression for

'correlation' given by the reviewer remains valid even for very short duration signals as a measure of similarity between the two deterministic (i.e., non-random) signals.

20. Reviewer's comment

Eq. (17): It may be worth specifying that $\overline{p^2}$ is function of both *r* and θ and that a cylindrical coordinate system (*r, θ, x*3) is used.

Authors' response

Thank you. We agree that this is confusing. We now write Eq. 17 for p^2 as a function of x1 and x2, and x3=0 and not θ as this will be introduced later on in the paper. For additional clarification, we now modify Eq. 17 as $p^2(x_1, x_2) = \cdots \ldots \ldots$"

21. Reviewer's comment

p. 19, l. 9: You are referring to $R_{\dot{B},\dot{F}}(-\tau_A)$ but it is $R_{\dot{F},\dot{B}}(-\tau_A)$ that appears in eq. (17).

Authors' response

Please note that by setting t=0 in Eq. 16, we obtain $R_{\dot{B},\dot{F}}(-\tau_A)$. However, by using the symmetry property, we obtain: $R_{\dot{F},\dot{B}}(-\tau_A)$which appears in Eq. (17). We hope that this is now clear?

22. Reviewer's comment

p. 19, l. 12: $\sigma = \sqrt{cos^2\theta + \beta^2 sin^2\theta}$
If the observer is assumed to be at *x*3 = 0, it might be worth mentioning it explicitly.

Authors' response: We now add on page 19 line 36 $x_2 = r\ sin\theta$ and x3 = 0.

23. Reviewer's comment
Eq. (18): I think there is a typo in the LaTeX code and that the equation should read:

$$\tau_A(\theta) = \frac{h}{c\beta^2}\left(M - \frac{\cos\theta}{\sqrt{\cos^2\theta + \beta^2\sin^2\theta}}\right)$$

Authors' response: Thank you. Now corrected.

24. Reviewer's comment

I think you may have expressed $-\tau_A$ instead of τ_A in eqs. (19) and (20). For eq. (19), I found …

Authors' response

The reviewer is correct. We are very grateful to the reviewer for pointing out this error, which was due to a change in sign convention made halfway through the project. This has now been corrected in Eqs 19 and 20, together with the plot in figure 12.

25. Reviewer's comment

Fig. 11: same remarks as for fig. 10 regarding the observer position and mention of dB scale.

Authors' response

We now specify that the mean square pressure directivity is in the *x*3 = 0 plane, plotted in dB

We now add the additional sentence,

"Figure 11 show those mean square pressure directives in dB in the x3 = 0 plane" .

26. Reviewer's comment

It may be a bit much to phrase it as "generally good agreement" for the directivity. But I think it is fair to say that the acoustic levels are relatively correct, except in the downstream direction. Have you tried to calculate the radiation from the baseline using a single compact source model at the leading edge (similar to your 2 sources model)? Maybe the noise reduction calculated from the difference between the compact source models (single source for baseline, 2 sources for slitted plate) can be compared to the noise reduction calculated from the difference between the numerical predictions.

Authors' response

We agree, it is a bit strong to say good. We now have changed this to "reasonably good agreement". We have considered your advice but we believe that an additional calculation based on a point leading baseline edge would add confusion. We hope that that the review is prepared for us to not make this change.

27. Reviewer's comment

p. 20 and fig. 12: On this page and this figure, you refer to (and plot) $R_{\dot{B},\dot{F}}(-\tau)$ but it is $R_{\dot{F},\dot{B}}(-\tau)$ that appears in eq. (17).

Authors' response

Thank you. We have looks at this issue carefully and have found that this is a typographical error. Figure 12 now has $R_{\dot{F},\dot{B}}(-\tau)$ plotted along the *y*-axis.

28. Reviewer's comment

p. 20, ll. 17-18: "... plotted against τ_A/τ_H think you mean plotted against τ/τ_H

Authors' response

Thanks you again. Yes, it should be τ/τ_H as τ_A is defined for the short interval between the two vertical lines. This is now corrected.

29. Reviewer's comment

Fig. 12: As mentioned earlier, here you plot the function $R_{\dot{B},\dot{F}}(\tau/\tau_H)$, but it is $R_{\dot{F},\dot{B}}(\tau)$ that appears in Eq. (17). This is confusing, since instead of looking for $R_{\dot{F},\dot{B}}(\tau/\tau_H) \leq 0$ for values of τ between $\tau_{A,min}$ and $\tau_{A,max}$, we need to find values of $R_{\dot{B},\dot{F}}(\tau/\tau_H) \leq 0$ for values of _ between $-\tau_{A,min}$ and $-\tau_{A,max}$,
On the figure, the vertical dotted lines seem to correspond to $-\tau_A(\pi)/\tau_H$ = −0.43 and $-\tau_A(\pi)/\tau_H$ = 0.23.
The values $2\Lambda/U$ appearing on the figure should be made non-dimensional in accordance with the x-axis ($2\Lambda/U\tau_H$?) Also, I think the x-axis should be labelled τ/τ_Hinstead of τ_A/τ_H

Authors' response

Yes, Many thanks again. There were three mistakes with this figure 12 that you correctly identified:

a. Should be τ/τ_H
b. Interval for τ_A/τ_Hincorrectly calculated
c. Should be $R_{\dot{F},\dot{B}}$ plotted along the y – axis.

All three errors now corrected. Thanks you.

30. Reviewer's comment

p. 21: in the text in this page, I think that every time you refer to τ_A/τ_H, you mean τ/τ_H.

Authors' response: Now corrected.

31. Reviewer's comment

p. 22: I think there is an error in your Fourier Transform identity after eq. (24). I think it should be:

Authors' response: Merci!. Whoever you are that was well spotted! Please let me know who you are so I can buy a beer! We have now made this correction. However, the final result remains unchanged.

32. Reviewer's comment

Eq. (25): As a consequence of my previous comment, the signs in the exponentials in this equation should be changed.

Authors' response: Yes, now changed!

33. Reviewer's comment

p. 23, l. 1: Are you sure about the signs in the exponentials for the expressions of $S_{B,F}(\omega)$ and $S_{F,B}(\omega)$? I think the signs should be opposite. Which would mean that, in the end, your eq. (26) is still correct.

Authors' response: Thank you! Signs now changed for consistency with Fourier transforms

34. Reviewer's comment

p. 24, ll. 11-15: "Clearly, therefore... back and front sources is significant." These sentences are not entirely clear to me. Could you please try to rephrase this part?

Authors' response

We mean that the mean square pressure, i.e., integrated overall frequencies, has a directivity that is controlled by the degree of correlation between their radiation, is therefore only weakly modified by interaction between the front and back sources. However, at a single frequency, strong interference effects are important and therefore the interaction between the front and back sources is therefore much more important.
After re-reading this sentence we believe the confusion originates from the redundant words "…. at all observer angles". This part of the sentence is now removed and we have modified the next sentence to say,
"This is in contrast with the mean square pressure directivity which is controlled only by the correlation between front and back sources"

35. Reviewer's comment

Fig. 14: Same remark as for figs. 10 and 11 regarding observer positions and dB scale. Also, I think θ_0 on fig. 14(a) should be about 73.

Authors' response

We now specify that the mean square pressure directivity is in the *x*3 = 0 plane, plotted in dB
We now add the additional sentence,
"Figure 14 shows the mean square pressure directives in dB in the x3 = 0 plane".

The angle θ_0 was incorrectly calculated – thank you. Figure 14a has been updated to show the correct angle of 73 degrees.

36. Reviewer's comment

Can you check this equation (28)?

Authors' response

Thank you so much again! Yes there was an error in the sign. This has been corrected!

37. Reviewer's comment

p. 27, l. 26: "... can be observed to vary smoothly and by less than 10dB over the frequency range." The front edge source strength varies by more than 10 dB over the frequency range in fig. 15.

Authors' response

We now change this sentence to,
"... can be observed to vary smoothly and by less than 12dB over the frequency range."

38. Reviewer's comment

p. 28, ll. 6-11: "For this particular... at f = 1.5 when they differ in phase by 3π. Maximum levels of noise reduction are therefore..." Is this 3π phase difference between the sources referring to $\omega\tau_H$? If yes, it may be nice to specify it here. Also, I understand the importance of the relative amplitude of the front and back edge sources to have significant interferences. But I am not sure as to why the value of $\omega\tau_H$ is important by itself, since for an observer it is the value of $\omega(\tau_H + \tau_A)$ that matters.

Authors' response

We agree that this section is confusing and potentially wrong. To obtain maximum noise reductions at any particular frequency and observer angle we need the source strengths to match when $\omega(\tau_H + \tau_A) = n\pi$. We have now completely modified this sentence. In describing figure 15 of the source strength spectra we remove any reference to the 3π phase difference.

We now explain that

"Figure 15 shows that the source strength are matching at fh/u=1.5 which is the frequency for which we obtain maximum noise on figure 14b at q1 for which the phase delay $\omega(\tau_H + \tau_A) = 3\pi$

39. Reviewer's comment

p. 28, ll. 11-13: "At the frequency of f = 0.5... suggesting relatively poorer levels of noise reduction at this frequency." I would maybe just rephrase it to specify that because of this difference in the two sources amplitudes, interferences effects are weak, thus we do not see observer positions where there are very strong noise reductions due to interferences between the two sources.

Authors' response

We agree that this sentence is not entirely clear. We have improved it to now say,

"At the frequency of f*=0.5, however, the source strengths can be seen to differ by about 8dB, suggesting relatively weak interference effects at this frequency. This prediction is consistent with the directivity plot of Fig. 14(a) at f*=0.5 in which poorer levels of noise reduction of around 10dB are observed and entirely attributed to a direct reduction in source strengths on the plate compared to the baseline case."

40. Reviewer's comment

Eq. (32): in this equation, I would just specify that S_{pp} also depends on θ and r, $S_{pp}(r, \omega, \theta)$

Authors' response: r and θ is now included

41. Reviewer's comment

p. 29, ll. 2-4: "The predicted sound power... obtained from the two-source model." Is the reduction for the two-source model calculated from the exact numerical prediction minus the two source model prediction?

Authors' response

We are unsure of the source of confusion in this question. The reduction for the two-source model is calculated from the difference of the power predicted from the two-source model – the baseline sound power. After re-reading the paper we believe this is sufficiently clear without further clarification.

42. Reviewer's comment

p. 29, l. 12: "... f* = 0.5, 1.5, 2.5 and 3.5..." I would remove the value f* = 3.5 from the list, since we do not really see much at this frequency

Authors' response: now corrected

43. Reviewer's comment

p. 30, l. 8: "... the interference between two compact sources..." I would just say "the interference between two sources". The compactness is an assumption of the two source model, but when compared to the exact numerical predictions, wee see (especially at angles downstream of the plate that the two sources are not really compact.

Authors' response: The word 'compact' is now removed

44. Reviewer's comment

p. 30, l. 8-11: "This paper has shown... interacting with the back-edge." See my previous comment on section 3.2.1 on secondary streamwise velocity. Also, doesn't the vortex original vorticity contribute to the back edge source?

Authors' response

We agree that this description should be clearer. Since drafting the original manuscript we have a clearer idea of the role of secondary vorticity on the noise reduction mechanism.

We have now amended this description in the conclusion, which now says,
"This paper has shown that the initial prescribed vortex impinging on the plate generates two sources at either end of the slits, whose levels are affected by secondary streamwise vortices originated at the slit corners and interacting with the front and back-edges of the slit."

45. Reviewer's comment

p. 30, l. 14: "Good agreement..." I would replace good by reasonable.

Authors' response: Done

46. Reviewer's comment

p. 31, ll. 1-2: "... that requires a much smaller modification to the leading edge than conventional serrations.". Do you mean smaller in terms of geometry (small slits)? If so, I am no sure that this is an argument by itself. The comparative effects of the slits in terms of aerodynamic performances (and eventually structural impacts) compared to conventional serrations should also be taken into account.

Authors' response

We have now modified this sentence to say
"…that requires a much smaller modification to the leading edge than conventional serrations in terms of the aerofoil area modification, However, their relative effects on aerodynamic performance and structural integrity remain to be determined. "

Typographical errors
These have all been modified – thank you.

***Author Style Checklist**

Journal of Sound and Vibration

Author Checklist

Authors should complete the following checklist and submit with their revised manuscript.

Math notation follows requirements on Guide for Authors (GFA) see: ☑

https://www.elsevier.com/journals/journal-of-sound-and-vibration/0022-460X/guide-for-authors

Use Roman (normal upright) type for: Total differential operators (e.g. d in differential); i or j (square root of -1); exp or e (base of natural logarithms); Re or Im (real or imaginary part); log, ln, sin, cos, etc.; abbreviations such as c.c. (complex conjugate); multiletter symbols (e.g. TL for transmission loss); subscripts of two or more letters identifiable as words or word-abbreviations (e.g., Apipe, fmax) ☑

For more unusual functions, JSV follows Abramowitz and Stegun's book. More detail given in the GFA (see link above).

Unit symbols - These should be upright (e.g. kg, not *kg*). ☑

All authors are listed on the manuscript with correct affiliations, correct email address and are in correct order. ☑

Keywords present. ☑

Manuscript is not currently submitted to any other Journal. ☑

If submitting highlights please note that only six may be submitted and each one should be no longer than 85 characters in length. ☑

Novelty of paper has been clearly stated in the Introduction. ☑

References are presented as per GFA. ☑

References not produced in English language to have English translation in brackets. ☑

Figures and Tables and Equations are numbered in sequence correctly. (See GFA). ☑

Nomenclature (if required) appears on second page of submission. ☑

Acknowledgements should appear in a separate section just after the conclusions. ☑

All abbreviations, in both the abstract and main body of document, are defined once only, the first time they appear in the text. (N.B. The Abstract is treated as an independent text, where references are given in full and abbreviations and symbols, if used, are properly defined.) ☑

Figures – if there are multi-parts to a figures each part is labelled (a) (b) (c) etc. and the labels defined in the figure caption. ☑

Figures – Colour can be used for the on-line version. Figures are reproduced in black and white in the printed journal and must therefore be readable in both colour and black & white. (N.B. charges apply for production of colour figures in the printed journal) ☑

Appendices – should appear before the list of references and labelled A, B, C, (please see GFA for further information regarding equations, figures and tables in the appendices. ☑

Copyright – material reproduced from other publications (e.g. Tables, Figures), source is acknowledged. ☑

List of the revisions made to the manuscript JSV-D-19-01748
By
Marine Cannard, Phillip Joseph, Paruchuri Chaitanya and Jae Wook Kim

All page and line numbers refer to the initial manuscript

Page 1 line 53
"occurs through the interaction between turbulent flow and the aerofoil leading-edge"

Page 2 line 33
"where U is the mean flow speed"

Page 2 line 49
"….. significantly better noise reductions than the conventional profile at low frequencies while generally providing smaller noise reductions at high frequencies due to trailing edge interaction [15]"

Page 2 line 54
"…… fh/U~ 0.5, 1.5 and 2.5. This condition implies a phase difference between two compact sources at either ends of the slit of pi, 3pi and 5pi. The most likely interpretation of this finding therefore is that the peaks are the result of destructive interference between these two sources". This hypothesis will be confirmed in the numerical surface pressure predictions presented below."

Page 5 line 29
σ and ϵ for the vortex parameters now changed to σ_{vortex} and ϵ_{vortex}

Page 6 line 28,
"…….. positive pressure is generated during the downward stroke *on the upper side of the* plate with the opposite behaviour occurring on the lower side"

Page 6 line 40:
"… the leading edge of the vortex is therefore assumed to be located at Λ from the vortex centre which is the initial position of the vortex, referred to as x_0 in Eq. (3)".

Page 8 line 19
There was a typo in this equation with the bracket ']' in the wrong place
e_t now corrected to $e_t = p/\rho(\gamma-1) + (u_j u_j)/2$. The equation refers to total energy and this is now made clear in the paper.

Page 9 line 46
"Note that, since the aerofoil is chord is essentially infinitely long no trailing edge correction was applied".

Page 10 line 24
The term $\beta^2 = 1 - M^2$ is now defined and the reference to the book "Aeroacoustics" by Goldstein (section 3,2) is now included to provide the derivation of the Green's function solution.

Page 13 line 19:
"….. as it is also the case for a straight leading edge aerofoil …."

Page 13 line 27:
"….. in the spanwise direction….."

Page 15 line 27:
"most of the span except close to the front corner where the streamwise vorticity is generated and therefore reaches comparable levels to the levels at the back."

Page 18 line 9
"Figure 10a and b shows those mean square pressure directives in dB in the $x_3 = 0$ plane".

Typo corrected in Equation 17
We now write Eq. 17 for p^2 as a function of x1 and x2, and x3=0 and not θ as this will be introduced later on in the paper. For additional clarification, we now modify Eq. 17 as $p^2(x_1, x_2) = \cdots \ldots \ldots$"

We now add on page 19 line 36 $x_2 = r\ sin\theta$ and x3 = 0.

Typo in Equation 18 corrected

Equation 19 and 20: sign was changed and plot in figure 12 is updated.

Page 20 line 35
"Figure 11 shows those mean square pressure directivity in dB in the x3 = 0 plane".

In all the text, τ_A/τ_H is replaced by τ/τ_H

Figure 12
There were three mistakes with that have been corrected:

a. Should be τ/τ_H
b. Interval for τ_A/τ_Hincorrectly calculated
c. Should be $R_{\dot{F},\dot{B}}$ plotted along the y – axis.

Error corrected in Fourier Transform identity after eq. (24)

Equation 25: signs in the exponentials in this equation have been changed.

Page 23 line 9
The signs in the exponentials for the expressions of $S_{B,F}(\omega)$ and $S_{F,B}(\omega)$ have been changed

Page 23 line 45
"Figure 14 shows the mean square pressure directives in dB in the x3 = 0 plane".
The angle θ_0 was incorrectly calculated – thank you. Figure 14a has been updated to show the correct angle of 73 degrees.

Page 24 line 50
"This is in contrast with the mean square pressure directivity which is controlled only by the correlation between front and back sources"

Equation 28 sign changed

Page 27 line 42
"... can be observed to vary smoothly and by less than 12dB over the frequency range."

Page 28 line 15-29
For this particular choice of slit dimensions (h and w) and choice of vortex size, the front and back edge source strengths can be observed to closely match at $f^* = 1.5$. Maximum levels of noise reduction are therefore predicted at this frequency, as shown in the directivity plot of Fig. 14(b), where sound pressure level reductions of up to 20dB are shown at the optimum angle θ_1, where the total phase delay $\omega(\tau_A + \tau_H)$ equals 3π. At the frequency of $f^* = 0.5$, however, the source strengths can be seen to differ by about 8dB, suggesting relatively weak interference effetcs at this frequency. This prediction is consistent with the directivity plot of Fig. 14(a) at $f^* = 0.5$ in which poorer levels of noise reduction of around 10dB are observed and entirely attributed to a direct reduction in source strengths on the plate compared to the baseline case.

Page 30 line 44
"This paper has shown that the initial prescribed vortex impinging on the plate generates two sources at either end of the slits, whose levels are affected by secondary streamwise vortices originated at the slit corners and interacting with the front and back-edges of the slit."

Page 31 line 9
"…that requires a much smaller modification to the leading edge than conventional serrations in terms of the aerofoil area modification, However, their relative effects on aerodynamic performance and structural integrity remain to be determined. "

New section added before conclusion: "Two-source model results for other slits configurations"
We now include four cases additional to the baseline case (h,w) of (2h,w), (h/2,w), (h,2w) and (h,w/2). A new figure 17 is now given comparing the predicted sound power level spectra, together with the predictions obtained from the two-source model.

In this section, we state that:

"The two-source model predictions can be observed to provide reasonable agreement with the exact calculation in all four cases, thereby validating the noise reduction mechanism proposed in this paper. Of the four cases, the case (h,w/2) gives the largest maximum noise reduction of 14.3 dB at $f^* = 0.5$ and the best overall noise reduction of 7dB. Clearly therefore, the noise reduction performance of the slit is highly sensitive to slit length and slit width. A complete parametric study is therefore required to identify the optimum slit parameters."

***Credit Author Statement**

Marine Cannard: Methodology, Investigation, Software **Phillip Joseph**: Supervision **Jacob Turner:** Software **Jae Wook Kim:** Software **Paruchuri Chaitanya:** Conceptualization

***Declaration of Interest Statement**

Declaration of interests

☒ The authors declare that they have no known competing financial interests or personal relationships that could have appeared to influence the work reported in this paper.

☐The authors declare the following financial interests/personal relationships which may be considered as potential competing interests: